

DOT/FAA/AR-01/124

Office of Aviation Research
Washington, D.C. 20591

Test and Analysis of Composite Sandwich Panels With Impact Damage

March 2002

Final Report

This document is available to the U.S. public
through the National Technical Information
Service (NTIS), Springfield, Virginia 22161.



U.S. Department of Transportation
Federal Aviation Administration

DISTRIBUTION STATEMENT A
Approved for Public Release
Distribution Unlimited

20020520 214

NOTICE

This document is disseminated under the sponsorship of the U.S. Department of Transportation in the interest of information exchange. The United States Government assumes no liability for the contents or use thereof. The United States Government does not endorse products or manufacturers. Trade or manufacturer's names appear herein solely because they are considered essential to the objective of this report. This document does not constitute FAA certification policy. Consult your local FAA aircraft certification office as to its use.

This report is available at the Federal Aviation Administration William J. Hughes Technical Center's Full-Text Technical Reports page: actlibrary.tc.faa.gov in Adobe Acrobat portable document format (PDF).

Technical Report Documentation Page

1. Report No. DOT/FAA/AR-01/124	2. Government Accession No.	3. Recipient's Catalog No.	
4. Title and Subtitle TEST AND ANALYSIS OF COMPOSITE SANDWICH PANELS WITH IMPACT DAMAGE		5. Report Date March 2002	
7. Author(s) R. Clif Moody and Anthony J. Vizzini		6. Performing Organization Code	
9. Performing Organization Name and Address University of Maryland Aerospace Engineering College Park, MD 20742		8. Performing Organization Report No.	
12. Sponsoring Agency Name and Address U.S. Department of Transportation Federal Aviation Administration Office of Aviation Research Washington, DC 20591		10. Work Unit No. (TRAIS) 11. Contract or Grant No.	
15. Supplementary Notes The FAA William J. Hughes Technical Center Technical Monitor was Mr. Peter Shyprykevich.		13. Type of Report and Period Covered Final Report	
16. Abstract Flat and curved (1.07-m radius) sandwich panels of various widths (83, 152, and 305 mm) were impacted and loaded uniaxially in compression until failure. Test results indicated that the width and curvature of the specimen had little effect on the ultimate strength. However, the point at which the impact damage grew as indicated by a nonlinear strain response was a function of the width and curvature of the specimen. An analytical formulation based on nonlinear deformations that included stiffness reduction, due to the impact, was able to model the nonlinear response of the specimens. The width and curvature affects the point at which the damage grows by resulting in varying stiffness in the facesheet. The formulation also indicates that the damage grew until it reached a critical size and arrested itself. This was observed in the experiments.			
17. Key Words Composite sandwich construction, Damage tolerance, Analysis models		18. Distribution Statement This document is available to the public through the National Technical Information Service (NTIS) Springfield, Virginia 22161.	
19. Security Classif. (of this report) Unclassified	20. Security Classif. (of this page) Unclassified	21. No. of Pages 67	22. Price

TABLE OF CONTENTS

	Page
EXECUTIVE SUMMARY	vii
1. INTRODUCTION	1
2. APPROACH	2
3. EXPERIMENTAL PROGRAM	3
3.1 Manufacturing	3
3.2 BVID Resolution	4
3.3 Damage Characterization	6
3.3.1 Nondestructive Evaluation of CAI Specimens	7
3.3.2 Damage Investigation of ID Specimens	8
3.4 Honeycomb Core Properties	15
3.5 Compression After Impact Testing	17
4. ANALYSIS	24
4.1 Section Property Analysis	24
4.2 Finite Element Analysis	26
4.3 Minguet/Tsang Model (Adapted)	29
4.3.1 Governing Equations	30
4.3.2 Equation Expansion	35
4.3.3 Substitution	42
4.3.4 Solution	47
4.3.5 Results	48
4.3.6 Required Input Parameters	53
4.3.7 Model Output	54
5. DISCUSSION	54
6. CONCLUSIONS AND RECOMMENDATIONS	58
7. REFERENCES	59

LIST OF FIGURES

Figure		Page
1	Sandwich Panel Layup	4
2	Impact Apparatus	5
3	Position of Curved Specimens	5
4	Forms of Impact Damage	6
5	Ultrasonic Scan of Impact Damage	7
6	Damage Size vs Panel Width	7
7	Type II Damage	8
8	Indentation Sampling Points	9
9	Maximum Residual Indentation Depth	9
10	Residual Indentation Shape—Type I Damage	10
11	Residual Indentation Shape—Type II Damage	10
12	Equations for Indentation Shape	11
13	Equation Accuracy	12
14	Size of Indentation Region	12
15	Orientation of Section Cuts	13
16	Size of Core Damage Region	14
17	Core Damage Depth	14
18	Compression Fixture for CP Tests	15
19	Out-of-Plane Stress-Strain Curve for Honeycomb Core	16
20	Properties of Honeycomb Core	16
21	Strain Gage Locations	17
22	Gripped Specimen	18
23	Potted Compression Test Fixture	19
24	Axial Direction Loading of Curved Panels	20
25	Failure Stresses of CAI Panels	21
26	Failure Stress vs Specimen Width for Damaged Panels	21
27	Damage Growth—Typical Gage-2 Data	22
28	Damage Growth Stress	22
29	Damage Growth Stress vs Specimen Width	23
30	Typical Gage-2 Data for Different Geometries	23
31	Section Property Models	25
32	Section Property Analysis Results	25
33	Geometry of Finite Element Model	26
34	In-Plane Load (N_x) in Front and Back Facesheet	27
35	Out-of-Plane Displacements of Front and Back Facesheets	28
36	Mid-Panel Displacement vs Damaged Region Compliance	28
37	Facesheet Loading Differential vs Damaged Region Compliance	29
38	Component of Damage in the Damaged Region	36
39	Regional Facesheet Compliance	37
40	Initial Shape of Facesheet	38
41	Simplified Stress-Strain Curve of Intact Core	39

42	Damaged Core Stress-Strain Curve	39
43	4 x 4 Sampling Points	42
44	Analytical vs Experimental Results	48
45	Model Width Effects on Damage Growth	49
46	Model Curvature Effects on Damage Growth	49
47	Model Membrane Damage Size Effects on Damage Growth	50
48	Model Bending Damage Size Effects on Damage Growth	51
49	Damage Arrest Mechanism	51
50	Out-of-Plane Deformation of the Flat 152-mm Model Without Facesheet Damage	52
51	Out-of-Plane Deformation of the Flat 152-mm Model With Facesheet Damage	52
52	Out-of-Plane Deformation of the Flat 83-mm Model Without Facesheet Damage	53
53	The Effect of Local Membrane Compliance on the Stress Concentration	56
54	Summary of Panel Behavior	57

LIST OF TABLES

Table	Page
1 Test Matrix	2
2 Strain Gage Locations	18

EXECUTIVE SUMMARY

A study of damage tolerance of composite sandwich panels was conducted with a focus on panels with thin facesheets and barely visible impact damage. The effects of specimen width and curvature on the compression after impact (CAI) behavior were of particular interest. Flat and curved (1.07-m radius of curvature) specimens of three widths (83, 152, and 305 mm) were impacted at a constant energy level (5.88 Joules). The extent of impact damage was found to be dependent upon the bending stiffness of the specimens. Each specimen was loaded in compression to failure with the CAI behavior recorded using strain gages. Test results demonstrated that width and curvature had little effect on the ultimate stress. The strain-gage data indicated that the stress at which the damage began to grow is a significant characteristic of the CAI behavior. The damage growth stress was defined as the stress at which the strain gage closest to the damage (25.4 mm) begins to show a nonlinear strain response to the loading. The test specimens with higher bending stiffness (which suffered more extensive damage) demonstrated a higher damage growth stress. Several analytical models were used to investigate the cause of the higher damage growth stress, first focusing on the effects of the global stiffness of the specimen, then concentrating on the local effects of the damage to the facesheet and core. The analytical model described here was successful in demonstrating the causes of the behavior seen in the testing and confirmed the importance of facesheet material damage.

1. INTRODUCTION.

Sandwich structures for aerospace applications in general consist of two thin, stiff, and strong facesheets (typically a composite laminate) separated by a thick, lightweight, and weaker core material (typically a foam or honeycomb). These types of structures offer a very high specific-bending stiffness. This is achieved through an optimized use of the system's components; in bending, the facesheets of the sandwich are loaded in membrane, for which they are best suited, and the core is loaded in shear. Sandwich structures are also good candidates for resisting in-plane compressive loads. Unlike traditional aircraft semimonocoque construction, the facesheets of the sandwich are supported out-of-plane over their entire area, reducing the effective column span and increasing the critical buckling load.

With widespread commercial use, the endurance and safety of sandwich structures becomes critically important. When used in real world environments, an aircraft structure is subjected to a wide variety of potentially damaging situations. Minor events such as tool drops, contact with service vehicles, and rock kick-up can cause significant damage to thin facesheet sandwich structures. The Federal Aviation Administration (FAA) has addressed aircraft structural damage issues in its Federal Aviation Regulations (FARs) and Advisory Circulars. The FARs require that the inspection intervals and procedures established for the aircraft prevent catastrophic failure of a structure containing an initial flaw of the maximum probable size that could exist as a result of manufacturing or service-induced damage. The residual strength and stiffness requirements are also addressed. The FARs include several flight regimes (load requirements) at which a damaged aircraft must be capable of performing. The FARs also require that the aircraft be capable of completing a flight after a damaging event from a discrete source, including bird strike and uncontained engine failure.

The research here was directed at determining the effects of the global geometry of the structure on the damage tolerance of composite sandwich panels. The focus of the research was sandwiches with thin facesheets and low-energy level impact damage. The overall objective of this program was to determine the consequences of using standard width flat specimens to represent structure of different geometries in damage tolerance studies. This was done by testing the compression after impact behavior of panels with different widths and curvatures.

In addition, several analysis techniques to model the behavior of the specimen under compressive load were proposed and compared to the experimental data. Initially, the elastic properties (in-plane and bending) of the various cross sections were determined to normalize the data. Subsequently, a coarse-mesh finite element model was developed to examine the load paths in a sandwich structure with stiffness degradation in one facesheet. The model provides an indication of the amount of load transferred to the back facesheet when the front facesheet is damaged. Finally, a nonlinear analysis is performed on an indented facesheet with stiffness degradation. This analysis provides a quick assessment of the growth of the indentation including the potential of arrest.

The work contained herein is organized in the following fashion. Section 2 defines the focus areas of this research and outlines the general approach used to investigate these issues. Section 2 also identifies the types of tests that were performed. All methods and results of the

experimental part of the program are included in section 3. Three analysis techniques are presented along with their results in section 4. The experimental data and the analysis methods are discussed in section 5. Section 6 contains the conclusions resulting from the experimentation and analysis as well as recommendations of additional research.

2. APPROACH.

The purpose of this investigation was to fill some of the current gaps identified in reference 1 in damage tolerance of thin-gage sandwich structures. The main objectives were (a) to examine sandwich panel geometries that more closely match those in the "real world," (b) to determine the significance of damage growth, (c) to investigate analytical methods that may be used to predict the onset of damage growth. All of these objectives can be related to determining the consequences of using a fixed-geometry coupon-level test specimen to determine the damage tolerance of global real-life structure.

This program focused on thin-gage facesheets, which is commonly used in the aerospace industry. The emphasis was on global geometry, and layups were kept constant for all specimens. All facesheets were built with a $[(90/0)]_s$ layup.

The damage levels used in the program correspond to what has been designated a barely visible impact damage (BVID). Aerospace structures are required to carry an ultimate load with damage that corresponds to the threshold of detectability (ToD) of the type of inspection method used. Commercial aircraft are typically inspected using visual methods. BVID is defined as the level of damage that can be detected by a visual inspection.

Four different types of test specimens were manufactured and tested: impact energy (IE) test specimens were used to determine the required impact energy to cause BVID in these particular materials, layups, and geometry; impact damage (ID) test specimens were used to investigate the type and amount of damage caused by the BVID impact event; core properties (CP) test specimens were used to establish the out-of-plane stiffness properties of the honeycomb core; and compression after impact (CAI) test specimens were used to investigate the damage tolerance of the panels after an impact event. The test matrix is given in table 1.

TABLE 1. TEST MATRIX

Flat/Curved	Size (mm)	Specimen Type			
		IE	ID	CP	CAI
Flat	51 x 51			6	
	83 x 356	20			16(4*)
	152 x 356		6		7
	305 x 356				7
Curved	152 x 356				7
	305 x 356				7

*indicates undamaged specimens

The analysis portion focused on different analysis techniques that may be applicable to predicting the growth of damage, in particular, methods that would give insight into the effects of global geometry on the damage growth stress.

3. EXPERIMENTAL PROGRAM.

An experimental program was conducted to study the effects of BVID on the compression strength of sandwich panels of different widths and curvatures. This section details the manufacture, inspection, and testing of the sandwich panels used for this program.

All test specimens were manufactured and tested at the University of Maryland's Composites Research Laboratory (CORE). The CORE lab provided all of the equipment required to manufacture the test specimens, including the clean room, autoclave, and three-axis milling machine. In addition, all testing equipment required was available at CORE.

3.1 MANUFACTURING.

The facesheets of the test specimens were built with an AS4/3501-6 graphite epoxy unidirectional preimpregnated system. The plies were cut to the required dimensions and laid up in a [(90/0)]_s configuration. Each facesheet was consolidated for at least 1 hour under vacuum prior to laying up the sandwich panel. The core material of the test specimens was a 48-kg/m³ phenolic (Nomex) honeycomb with 3-mm cells. In some baseline specimens, an 80-kg/m³ aluminum honeycomb was used in the gripped ends of the specimens. The facesheets and core were assembled together after placing a layer of FM-300 film adhesive between the core and the uncured facesheets.

The facesheets were cured and bonded to the core concurrently (co-cure). This method mimics the manufacturing practices of the aerospace industry. The manufacturer's recommendations of a cure at 177°C were followed with one exception; a reduced autoclave pressure of 276 kPa was used during the cure so as not to crush the core material. A curved aluminum cure plate (1.07-mm radius of curvature) was used for the axially curved panels. Aluminum bars were placed around the free edges of the uncured panels. This prevented the pressure from the vacuum bag from damaging the core at the edges of the specimen (figure 1).

Several of the panels were nondestructively examined following the cure cycle. NASA Goddard Space Flight Center provided a pulse-echo ultrasonic scanning machine at their facility. Postcure scans of these panels allowed for the detection of voids or debonds in the facesheets and/or other problems caused by inadequate manufacturing or curing process. This procedure validated the established processes and provided quality control.

Once cured, the panels were cut to the determined specimen size using water-cooled diamond saw tooling. The number and size of each type of test specimen created is shown in table 1.

Because the honeycomb core was subjected to water during both the cutting (water-cooling) and the inspection (water stream for ultrasound), all specimens were placed in an environmental chamber with low humidity and mild heat to remove any moisture from the core material.

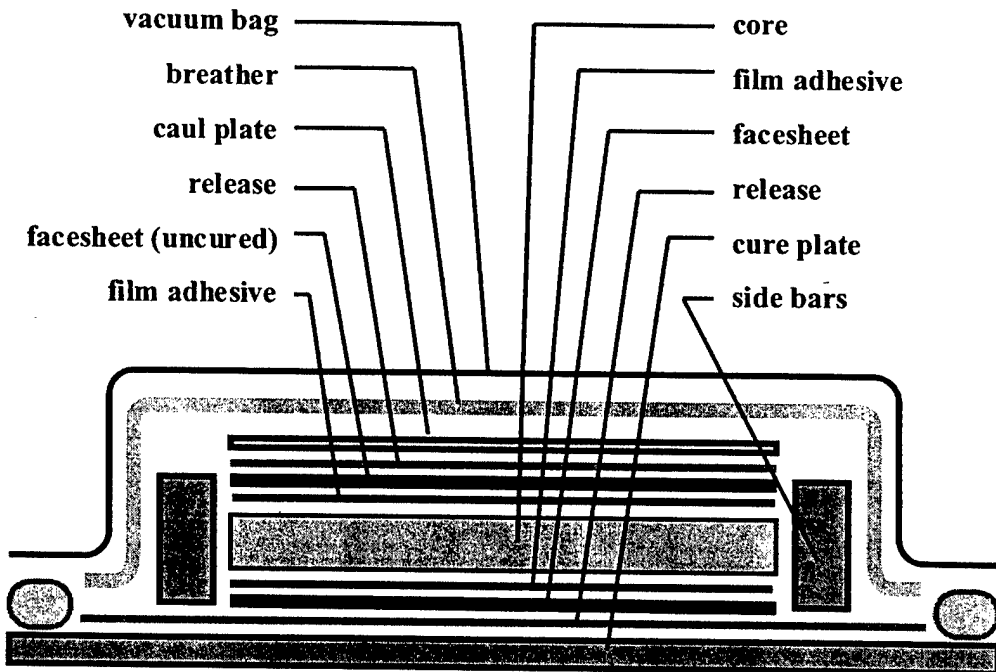


FIGURE 1. SANDWICH PANEL LAYUP

3.2 BVID RESOLUTION.

Low-energy impact that does not cause penetration is of a particular concern in the design of aircraft primary structures. BVID is defined as the damage level corresponding to the ToD for a visual inspection. Kassapoglou quantified BVID with his specification: "...the indentation left by the impact and the associated local damage is barely visible from a distance of about 120 cm" [2]. This definition is used throughout this program.

Impact damage was inflicted upon the test specimens using a drop tower with a 25.4-mm-diameter stainless steel hemispherical tup (figure 2). The impact apparatus had a mass of 1.31 kg. The specimens were clamped across their width (top and bottom) resulting in a span of 229 mm. The curved panels were positioned so that their axis of curvature was in the direction of the span (figure 3). All specimens were impacted at their center. The impactor was arrested after impact to halt the rebound so that only the initial drop impacted the specimens. The energy of the impact was measured as the total potential energy of the system before impact, ignoring frictional losses during the drop and energy of the rebound, as defined in equation 1.

$$E = W \times h \quad (1)$$

where:

- E : energy of the impact event
- W : weight of the impactor
- h : drop height

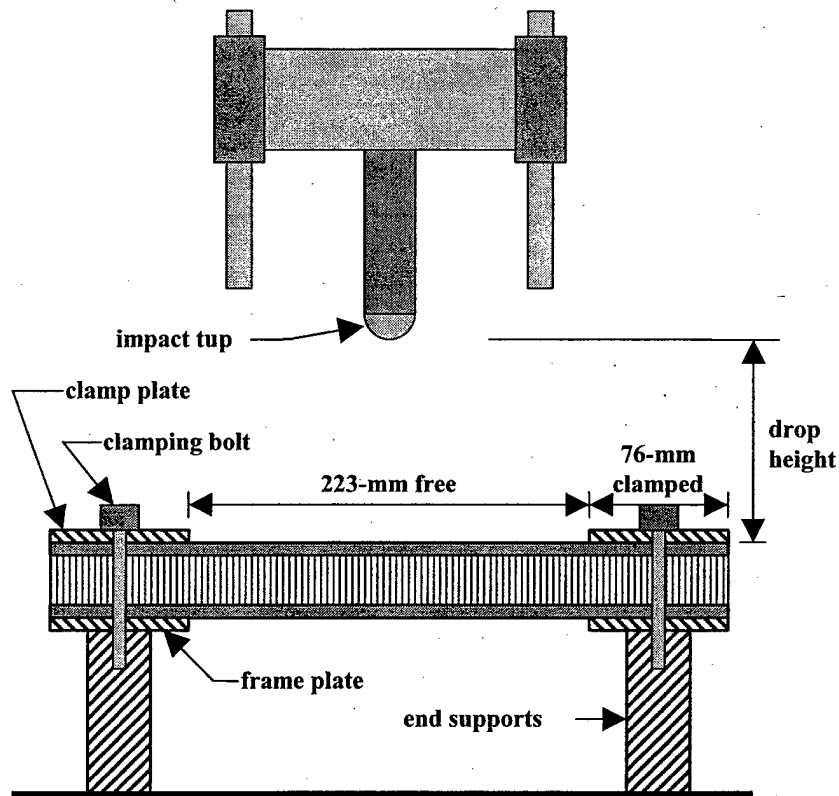


FIGURE 2. IMPACT APPARATUS (Drop tower)

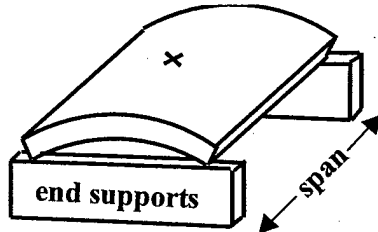


FIGURE 3. POSITION OF CURVED SPECIMENS

To determine the energy level required to cause BVID, the 20 IE test specimens were impacted with increasing energy levels by increasing the drop height for each test (maintaining constant impact apparatus mass). Using the method recommended by Kassapoglou [2], all impacted specimens were visually examined from 120 cm and the impact energy causing BVID was established. For this program, the BVID energy level was determined to be 5.88 J (drop height of 457 mm). The velocity of this impact was approximately 3.0 m/s.

The impact energy determined to cause BVID in the IE test specimens was used for all remaining impacted specimens in the program. The BVID observed was typically a very small indentation on the order of the thickness of the facesheet (depth of 0.5 mm). In some cases, there was apparent matrix cracking and fiber breakage, other damaged panels exhibited only a small residual indentation caused by the impact event.

3.3 DAMAGE CHARACTERIZATION.

To gain insight into the behavior of the damaged panels under compression, it is important to understand the effects of the impact on the sandwich panel. Low-energy impact causes several complicated types of damage to thin-gage facesheets of sandwich structures (figure 4). At very low energy levels, the impactor deflects the surface and the facesheet rebounds. There is no visible damage to the panel; however, the cell walls of the core are crushed (buckled) and pulled back up with the facesheet. While the facesheet may be undamaged at this stage, it is unsupported by the core at the impact area and is subject to local buckling. Higher energy impacts cause the facesheet to have a permanent indentation at the impact site. This indentation and the associated core damage can cause local instability in compression. Delamination and disbond can also occur between the plies of the facesheet. Typically, the largest delamination is between the innermost ply and its neighbor. Damage to the facesheet can be in the form of matrix cracking and fiber breakage. These types of damage can cause a reduction in the stiffness and strength of the facesheet. In addition to the several types of damage that can occur during an impact, the regional effects of the damage are also important. Near the center of the impact, the facesheet damage and core crushing will be highest, with a gradual decrease away from the center.

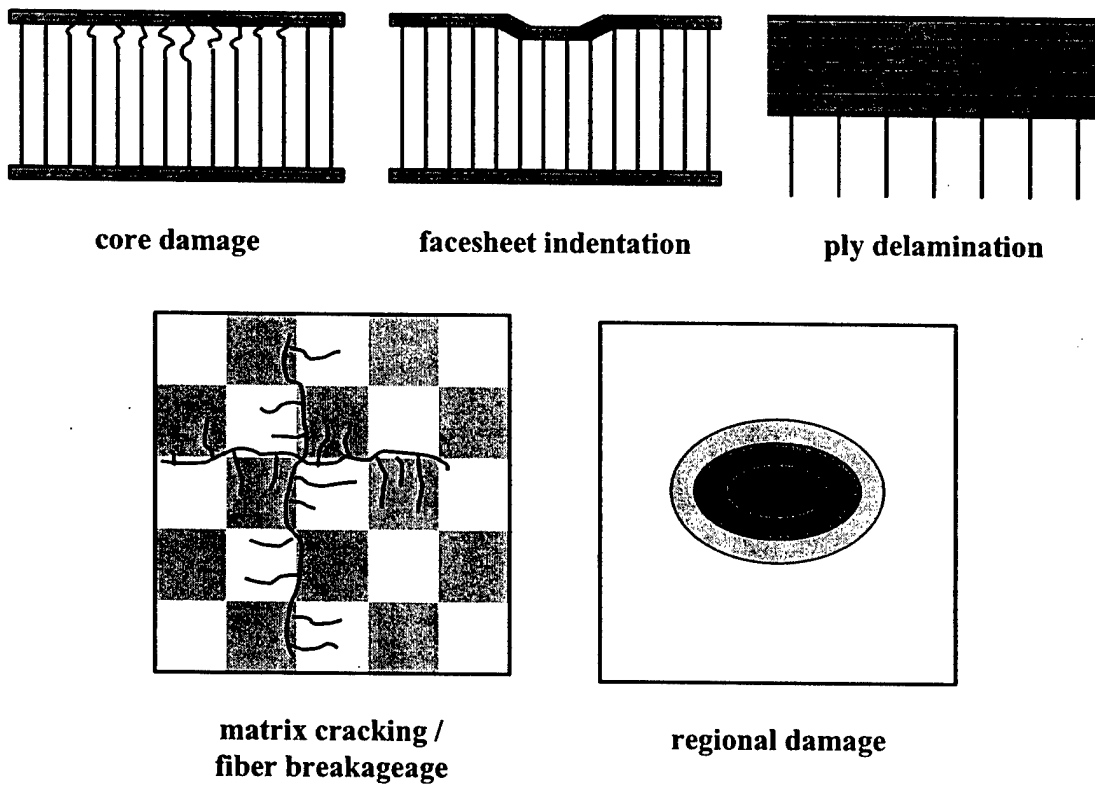


FIGURE 4. FORMS OF IMPACT DAMAGE

Impact damage can be characterized into three types: facesheet damage (residual indentation), facesheet material damage (ply delamination, matrix cracking, and fiber breakage), and core damage [3].

The impact damage observed in this investigation included all of the above forms, to some extent. The many forms of the damage present, make modeling the damage region difficult. Individual simplifications such as loss in stiffness, equivalent delamination, or residual indentation may not capture all of the damage mechanisms that are required for an accurate analysis of the compression after impact behavior.

3.3.1 Nondestructive Evaluation of CAI Specimens.

To nondestructively evaluate the damaged region, a second ultrasonic investigation was performed to determine the amount of internal damage within the facesheet of the sandwich panel. The results from the scan show the overall size of the elliptical damage area (figure 5). The shadings of the ultrasonic scans represent either a residual indentation left after the impact or a delamination between the plies of the facesheet.

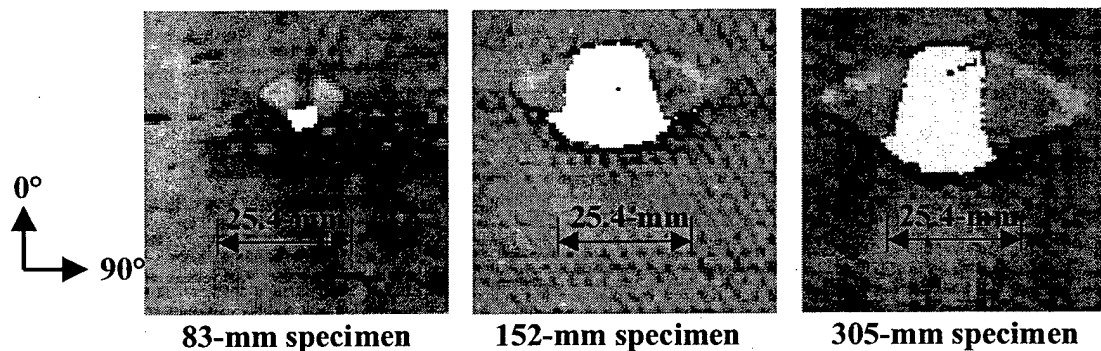


FIGURE 5. ULTRASONIC SCAN OF IMPACT DAMAGE (3 widths)

The ultrasonic inspections demonstrated that the wider panels exhibit larger damage areas (figure 6). The higher stiffness of the wider panels resulted in less energy being absorbed in global bending and more energy being absorbed in local damage. This is an indication of damage resistance being dependent upon the global stiffness of the panel, which is an important observation for scaling the results of coupon tests to full scale aircraft structures.

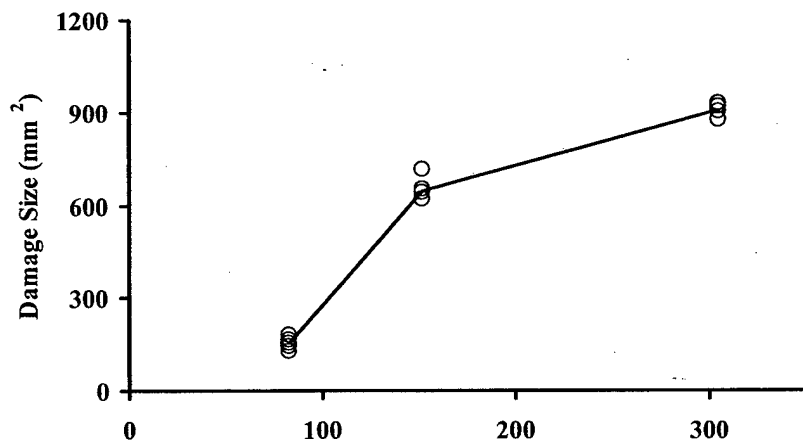


FIGURE 6. DAMAGE SIZE VS PANEL WIDTH

While the ultrasonic inspection gave some insight into the general size of the impact damage region, this method did not reveal any information concerning the specific features of the damaged facesheet. There was no indication of the extent of core or facesheet damage.

3.3.2 Damage Investigation of ID Specimens.

To gain more insight into the actual damage mechanisms resulting from the impact event, several panels were impacted and sectioned. Six ID test specimens were impacted with the established BVID energy level. Both sides of these panels were impacted resulting in 12 damage region samples.

The damage caused to the ID panels by the impact event can be divided into two types. One type of damage results in no apparent facesheet damage (type I). Examination of the surface of these panels shows no matrix cracking or fiber breakage, only a residual indentation left by the impact. The second type of impact damage causes obvious damage to the matrix and fibers of the facesheet (type II). There exists a varying degree of fiber breakage in the top (90°) ply as well as through thickness cracks in the laminate (figure 7). Four of the twelve ID specimens displayed type I damage, the remaining eight showed type II damage.

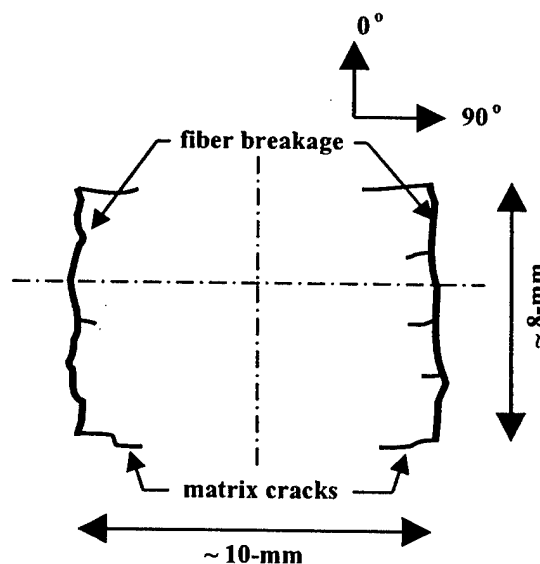


FIGURE 7. TYPE II DAMAGE

The shape and size of the indentation left by the impact event seemed to be a significant factor in the compression failure behavior of the panel. The residual out-of-plane displacement of the facesheet was measured at specific points using a dial gage and the table of a milling machine. The dial gage was used to measure the out-of-plane location of the facesheet, while the milling machine table provided for an accurate measurement of the in-plane location of the dial gage probe. The ID specimens were placed flat on the table, the in-plane location zeroed at the center of the impact zone. Dial gage readings were recorded at points along the width and length of the panel (figure 8).

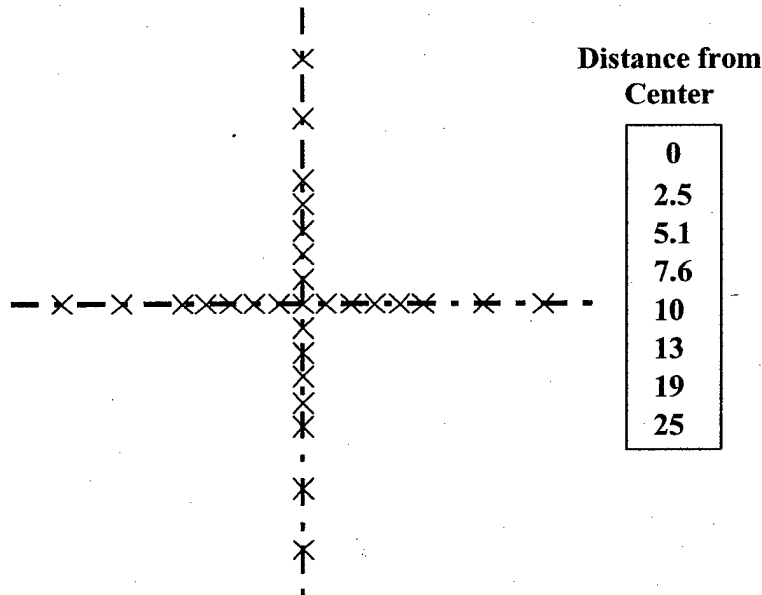


FIGURE 8. INDENTATION SAMPLING POINTS (mm)

The maximum depth of the residual indentation is determined from the out-of-plane displacement data, measured at the center of the damage area (figure 9). In this figure, the single lines at the top of the columns represent the spread of the experimental data. Above each column is a number (%) representing the coefficient of variation of the experimental data. The average maximum indentation depth did appear to have some dependence on the damage type.

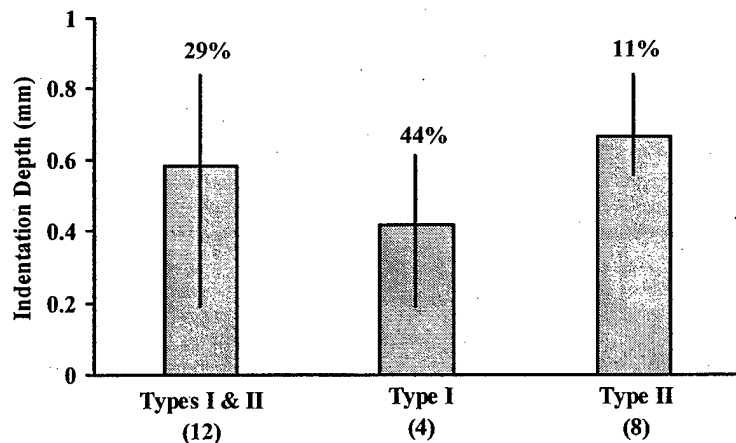


FIGURE 9. MAXIMUM RESIDUAL INDENTATION DEPTH

The surface measurements also revealed the general shape of the residual indentation left after impact (figures 10 and 11). In general, the region of the indentation is slightly wider than it is long (due to the orthotropic nature of the facesheet). The shape of the indentation appears to be similar for both damage types.

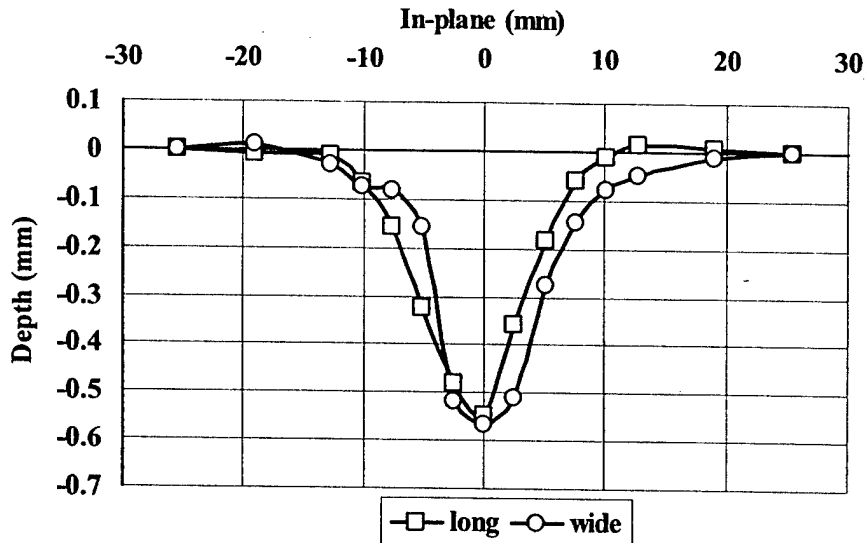


FIGURE 10. RESIDUAL INDENTATION SHAPE—TYPE I DAMAGE

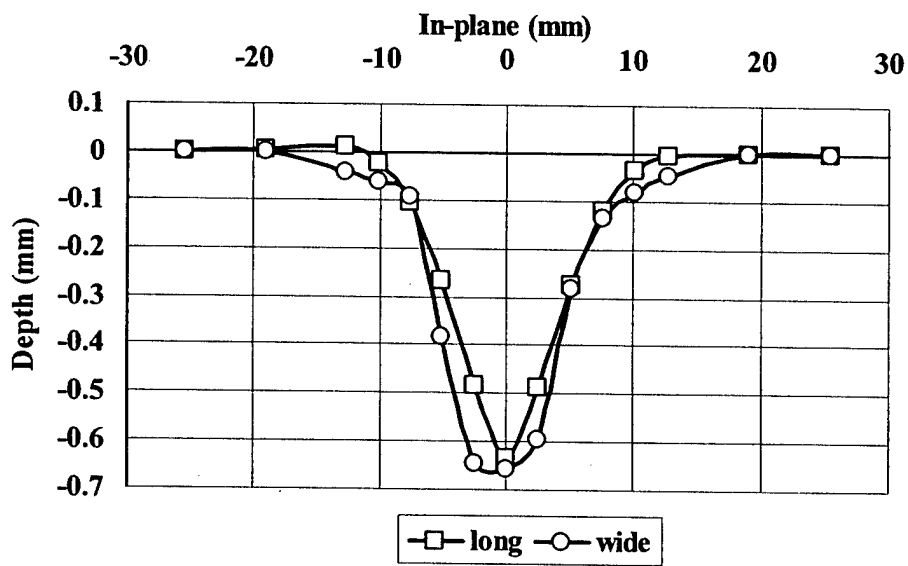


FIGURE 11. RESIDUAL INDENTATION SHAPE—TYPE II DAMAGE

For modeling purposes, it is desirable to match the shape corresponding to the residual indentation to a simple equation. Minguet [4] recommended a cosine-squared term to describe the indentation (equation 2). This equation seems to give a less “steep” shape than the actual measured data from the panel damage. A higher order cosine term appeared to match the measured curve more closely (figure 12). A quantitative value, which describes the accuracy of the equation by comparing the predicted and measured values for the out-of-plane location of the facesheet, is used to find the appropriate power (equation 3). Based on the resulting accuracy curve (figure 13) a cosine⁸ term (equation 4) was chosen for this program.

$$\xi(x,y) = \xi_0 \cos^2 \left[\frac{\pi \left(x - \frac{a}{2} \right)}{2R_{dent,x}} \right] \cos^2 \left[\frac{\pi \left(y - \frac{b}{2} \right)}{2R_{dent,y}} \right] \quad (2)$$

where:

ξ, ξ_0 : residual out-of-plane displacement of the facesheet resulting from the impact event, depth at the center of the impact region

a, b : width, length of the panel

$R_{dent,x}, R_{dent,y}$: radius of the indentation region in the x, y direction

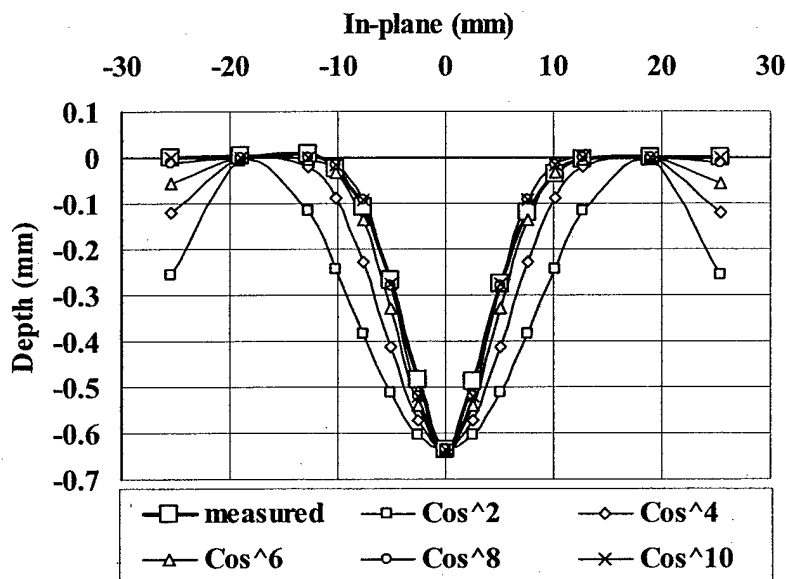


FIGURE 12. EQUATIONS FOR INDENTATION SHAPE

$$Acc = 1 - \sqrt{(z_1^e - z_1^m)^2 + (z_2^e - z_2^m)^2 + \dots + (z_3^e - z_3^m)^2} \quad (3)$$

where:

Acc : calculated accuracy value

z_1^e : out-of-plane displacement as determined by the equation

z_1^m : out-of-plane displacement as measured

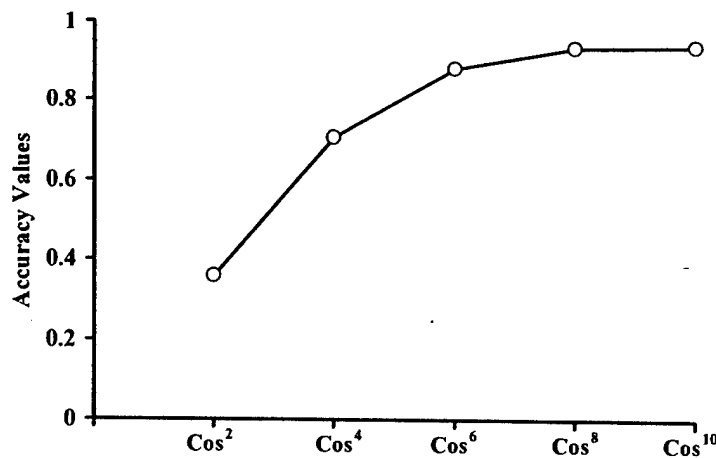


FIGURE 13. EQUATION ACCURACY

The sizes (width and length) of the indentation regions can be determined using equation 4, by solving for the $R_{dent,x}$ and $R_{dent,y}$ that results in the highest accuracy values. The indentation radii were determined for all damage regions (figure 14). The average damage region length is approximately 95% of the average damage region width, showing the effect of the directional stiffness of the facesheet. Both type I and type II damage demonstrated similar indentation widths and lengths.

$$\xi(x,y) = \xi_0 \cos^8 \left[\frac{\pi(x-a)}{2R_{dent,x}} \right] \cos^8 \left[\frac{\pi(y-b)}{2R_{dent,y}} \right] \quad (4)$$

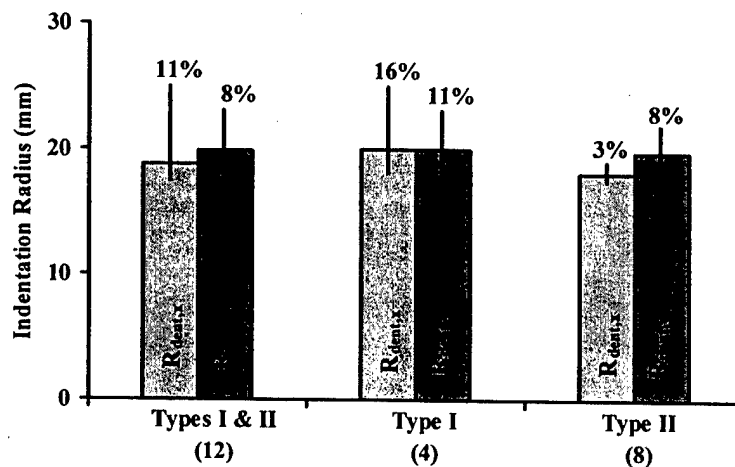


FIGURE 14. SIZE OF INDENTATION REGION

All of the ID specimens were sectioned along the centerline to examine the damage caused to the facesheet (delamination and cracking), the core (crushing), and the adhesive layer (disbond). The section cuts were made with water-cooled diamond saw tooling. To look at the extent of damage in both the longitudinal and transverse directions, cuts were made in two different ways as shown in figure 15.

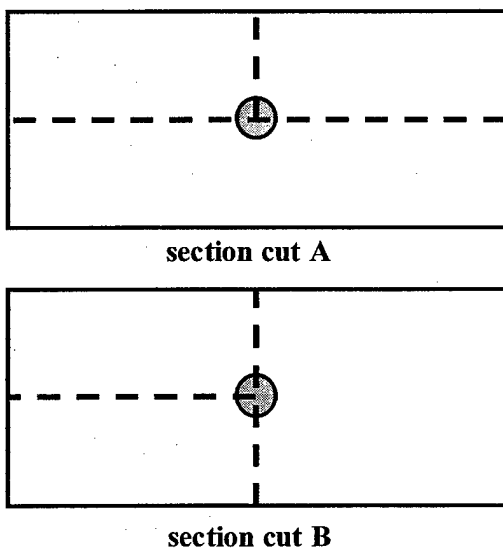


FIGURE 15. ORIENTATION OF SECTION CUTS

The section cuts to the ID panels revealed the extent of damage in the honeycomb core. During an impact event, the facesheet will deflect under the impact device, buckling the cell walls of the core below. After the impact, the facesheet will rebound and approach the original shape of the panel, pulling up the attached cell walls. The core material immediately below the impact zone was crushed with extensive cell wall buckling. Away from the impact center, there remained evidence of core damage. Cell wall waviness and discoloration indicated cell walls that had been crushed during the impact and then rebounded after the event. The residual indicators of core damage were used to measure the extent of core damage in the impacted panels. The length and depth of the apparent damage was measured in both the longitudinal and transverse directions with a 1-mm resolution. A stereoscope was used to assist in the measurements.

The type of facesheet damage (I or II) did not have a significant effect on the size of the core damage region (figure 16). The damage region is approximately 43% wider than it is long. This is expected due to the higher bending stiffness of the facesheet laminate in the transverse direction. The maximum depth of the core damage did show some dependence on visible damage type (figure 17). The core damage depth of the type I facesheet damage is approximately 17% less than the core damage depth of the type II facesheet damage. This can be explained by the nature of the two damage types. The type I damage absorbs more of the impact energy in elastic bending of the facesheets (maintaining some integrity), while the type II damage absorbs some energy in the bending and breaking of the facesheets and the remaining energy in the deflection of the core.

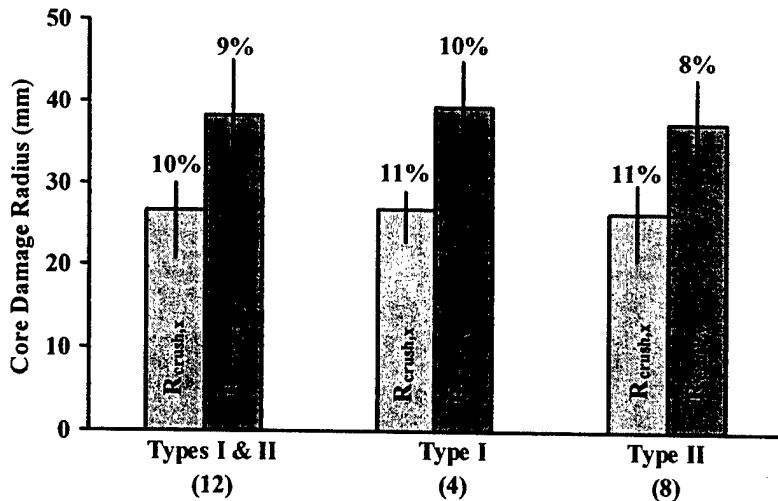


FIGURE 16. SIZE OF CORE DAMAGE REGION

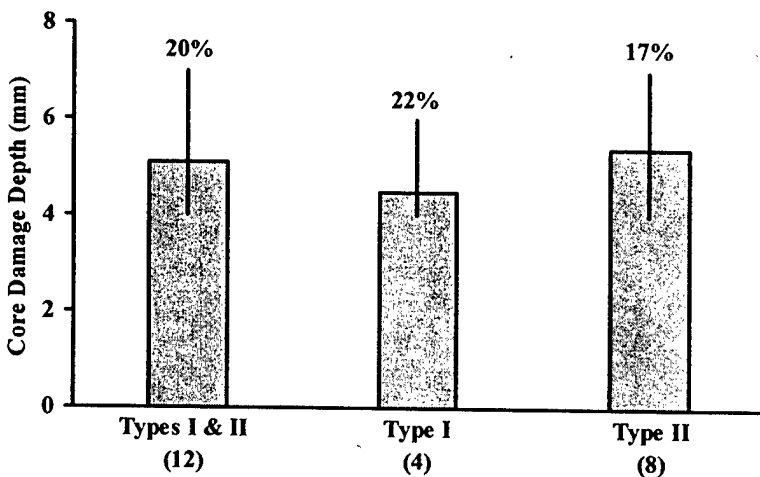


FIGURE 17. CORE DAMAGE DEPTH

The impact damage to the facesheet was apparent after sectioning the specimens. Damage forms observed included delaminations, matrix cracking, and ply failure (fiber breakage). The delaminations typically occurred between the innermost ply and its neighbor (between plies three and four). The delaminations observed were more extensive in the transverse direction. The second and third plies of the damaged facesheet typically showed matrix cracking between the fibers. These matrix cracks were visible in the transverse sections. In addition, the innermost ply typically had a through-thickness crack in the matrix parallel to the fiber direction. This crack was visible in the longitudinal sections. Some of the specimens showed fiber breakage in the top ply of the facesheet (type II damage). These damage mechanisms typically occurred at each side of the impact center and were visible in the transverse sections. The extent of facesheet damage was measured in all panels with the help of a stereoscope. Typically, the damage was limited to a width of 30 to 50 mm and a length of 5 to 13 mm.

3.4 HONEYCOMB CORE PROPERTIES.

The stiffness properties of the honeycomb core are important factors in the compression behavior of sandwich panels. Euro-Composites (the core manufacturer) provided some properties for a stabilized Nomex honeycomb core:

$$\sigma_{zz}^{ult} = 1.9 \text{ MPa}$$

$$E_{zz}^{elastic} = 138 \text{ MPa}$$

However, the behavior of the core, beyond the ultimate load, has been shown to have significant influence on the compression after impact behavior of sandwich panels. Typically, Nomex honeycomb core will have a linear stress-strain relationship up to the ultimate out-of-plane load. At this point, the cell walls of the core will buckle and the load-carrying capability of the core will drop significantly.

To measure the nonlinear out-of-plane compression properties of the core used in this program, six 51- by 51-mm test specimens were cut from cured sandwich panels (with facesheets). These specimens were placed between two aluminum plates in the uniaxial testing machine (figure 18). Loading of the specimens was stroke controlled with a ramp rate of 0.032 mm/s. The heads of the testing machine compressed the specimen until the total stroke reached 6 mm. At this point, the direction of the stroke was reversed and the specimen was unloaded.

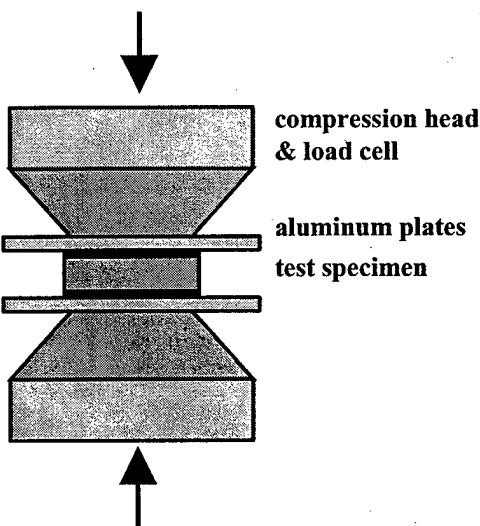


FIGURE 18. COMPRESSION FIXTURE FOR CP TESTS

Before ultimate stress was reached, the panel had a near linear elastic response to the out-of-plane load (figure 19). At the ultimate stress, the cell walls of the honeycomb core buckled at the mid-plane region of the core. The total stress in the specimen dropped to approximately 50% of the ultimate stress. Additional displacement resulted in only a slight increase in the stress in the core as the cell walls continued to buckle. At a displacement of 6 mm, the unloaded panel showed an initially linear rebound back to zero stress.

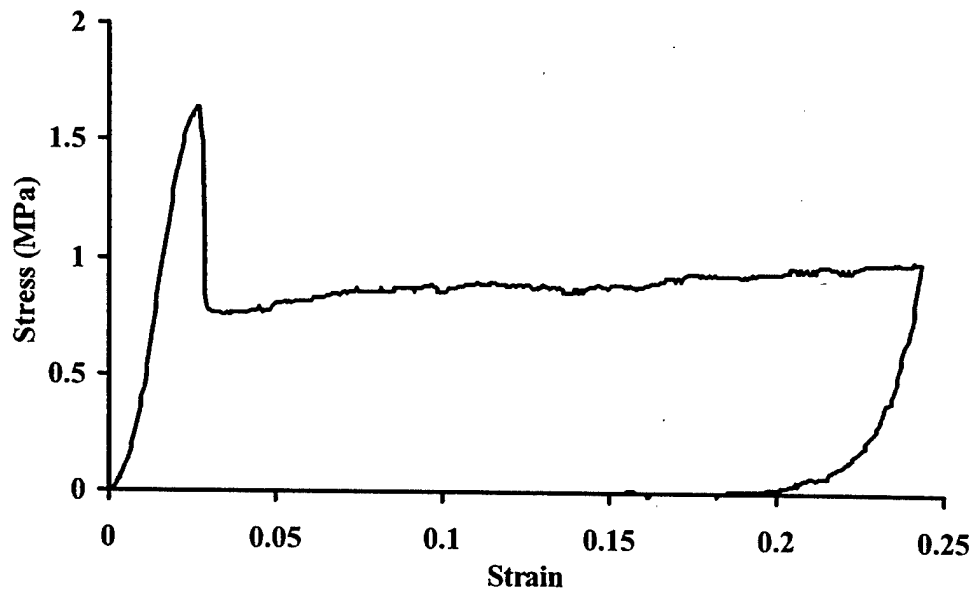


FIGURE 19. OUT-OF-PLANE STRESS-STRAIN CURVE FOR HONEYCOMB CORE

From the six tests, the mean out-of-plane modulus of the core material (before ultimate load) was 295 MPa (figure 20). The mean ultimate stress and plateau (drop-off) stress were 1.72 MPa and 0.791 MPa (46% of the mean ultimate). The mean rebound modulus was 227 MPa (77% of the elastic modulus).

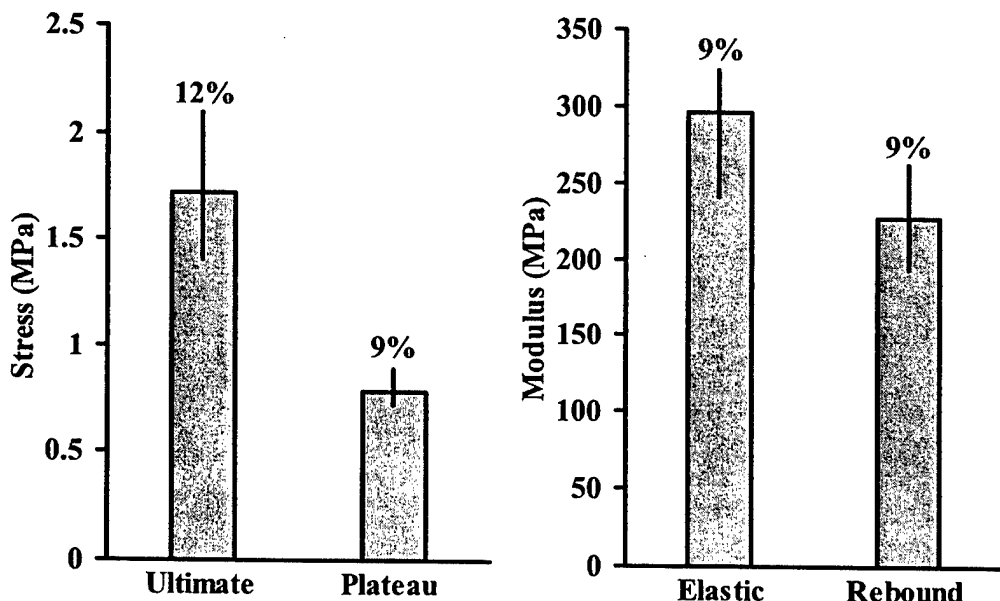


FIGURE 20. PROPERTIES OF HONEYCOMB CORE

3.5 COMPRESSION AFTER IMPACT TESTING.

The CAI specimens were tested to study the effects of global geometry. Strain gages were affixed to the specimens to capture the response of the test specimen under compression. The strain gage locations were chosen to measure the behavior of the panel under increasing load (figure 21 and table 2). Far-field gages were placed away from the damage on the front and back facesheet in order to capture any load-carrying differential between the facesheets due to the damage. To capture the lateral propagation of the damage indentation, gages were also placed on the front facesheet, perpendicular to the damage. Gages placed on the back facesheet, behind the damaged region, measured the local-load transfer to the back facesheet near the damage.

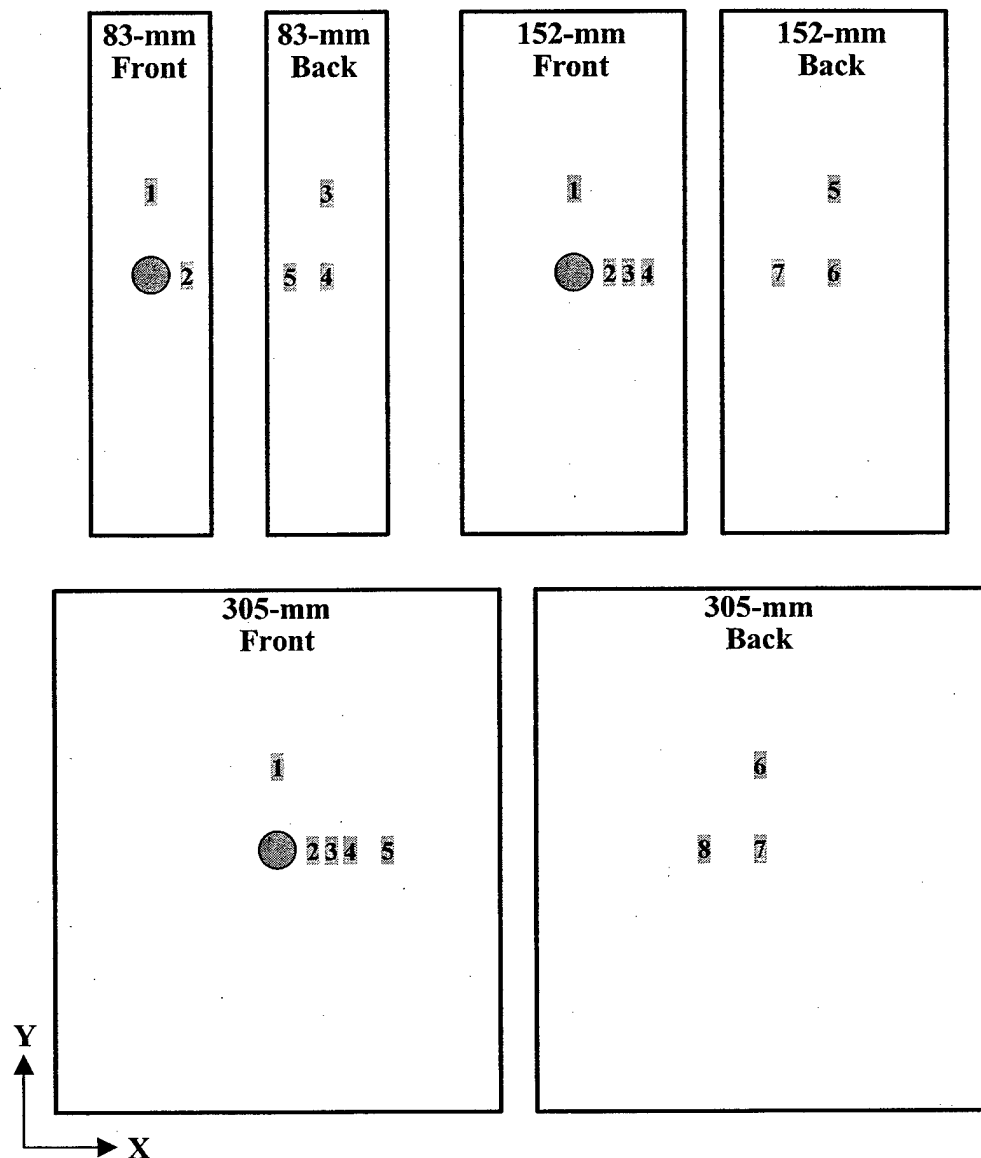


FIGURE 21. STRAIN GAGE LOCATIONS

TABLE 2. STRAIN GAGE LOCATIONS (mm)

Gage	83-mm		152-mm		305-mm	
	X	Y	X	Y	X	Y
1	0.0	76.2	0.0	76.2	0.0	76.2
2	25.4	0.0	25.4	0.0	25.4	0.0
3	0.0	76.2	38.1	0.0	38.1	0.0
4	0.0	0.0	50.8	0.0	50.8	0.0
5	-25.4	0.0	0.0	76.2	76.2	0.0
6			0.0	0.0	0.0	76.2
7			-38.1	0.0	0.0	0.0
8					-38.1	0.0

The 83-mm CAI specimens in this program were tabbed and gripped in the uniaxial testing machine. To prevent the grips from crushing the soft Nomex core, an aluminum core was used in the gripped ends of the 83-mm specimens (figure 22).

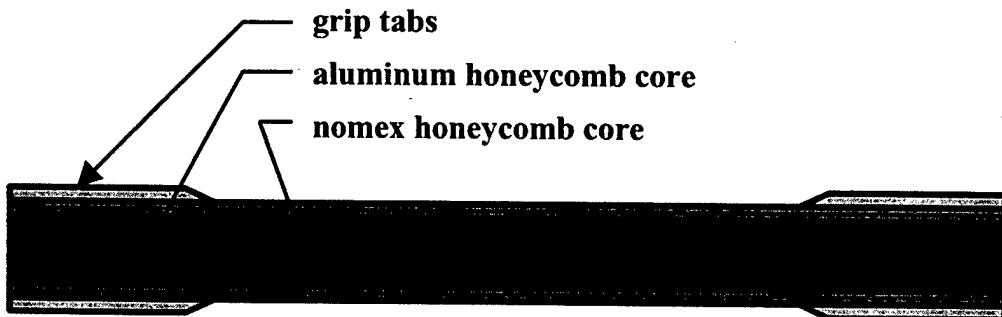


FIGURE 22. GRIPPED SPECIMEN

The grips of the testing machine are limited to a width of approximately 83 mm. An alternative gripping system had to be used to test specimens wider than 83 mm. Typically, the ends of wider specimens are potted in an epoxy resin. The hardened resin is then machined to fit the grips of the testing machine. This method has several disadvantages in that the resin permanently alters the test specimen so that handling after testing is difficult and also requires time-consuming machining operations before each test.

Some investigation went into the development of an alternative gripping system for the wide panels. A cerro-bismuth metal alloy with a low melting temperature (70°C) was used to pot the ends of the specimens. The relatively low melting temperature of the potting material did not damage the composite facesheets of the specimens. Once tested, the specimens were easily removed from the potting material with the application of heat.

Aluminum and steel end molds were used as potting forms (figure 23). These end forms were designed to accommodate any width of specimen up to 305 mm and thicknesses up to approximately 38 mm. End forms also allowed for some degree of curvature. Steel side plates were used to align the end forms before potting and to prevent inadvertent loading and damage to the specimens during handling prior to the test.

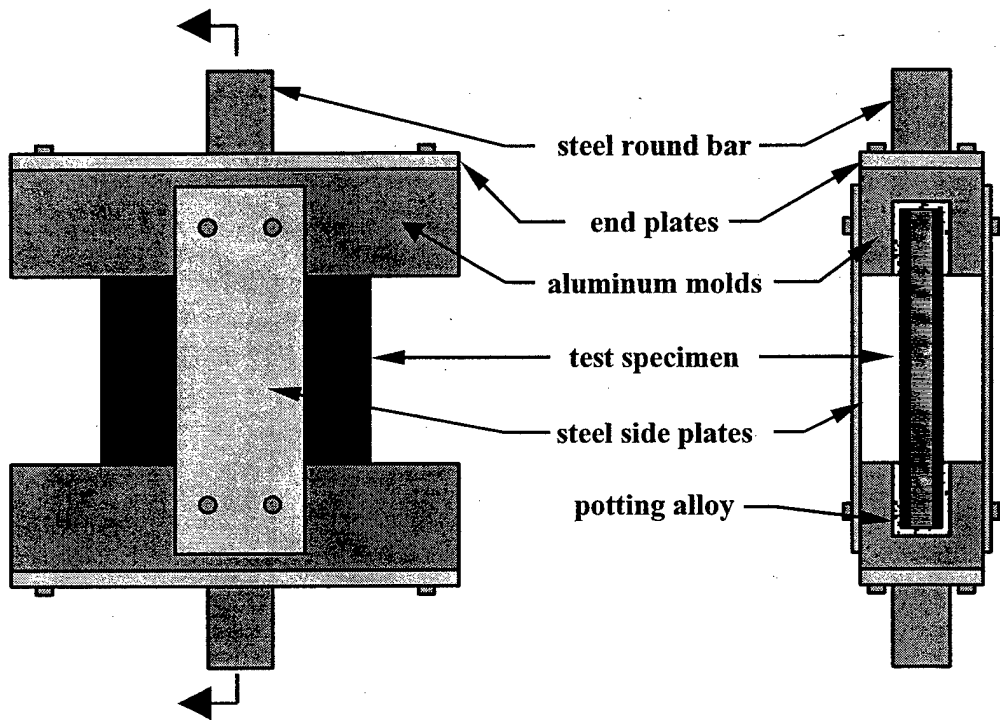


FIGURE 23. POTTED COMPRESSION TEST FIXTURE

The specimens were potted by first aligning the end molds parallel to one another and fixing them together by tightening the side plates. The specimen was then centered in the molds using shims and restrained with tape. The end form that was to be potted first was heated to approximately 71°C to prevent the potting material from cooling rapidly during the pour and creating voids in the forms. The heated potting material (approximately 82°C) was then poured into the form and around the specimen. The mold was filled approximately 75% and allowed to cool. A second pour filled the remaining part of the form and resulted in an adequate end condition. Most of the loads, from handling, were absorbed by the steel side plates. This potting method resulted in fixed-end conditions leaving a 203-mm column length.

All CAI specimens were loaded in an uniaxial testing machine. Steel round bars were gripped in the diamond-shaped grips of the testing machine. The loading was stroke (displacement) controlled with a ramp rate of 0.05 mm/s resulting in a strain rate of 250 $\mu\text{e/s}$. Strain gage, stroke, and load data were collected at 0.2 s intervals. The curved panels were loaded in the axial direction as shown in figure 24.

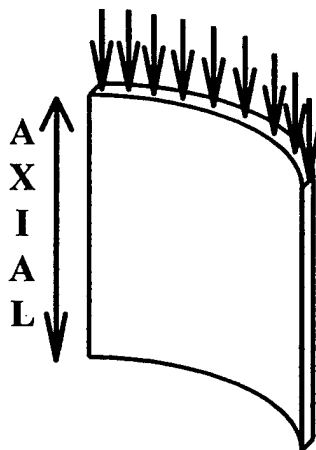


FIGURE 24. AXIAL DIRECTION LOADING OF CURVED PANELS

All specimens were loaded to failure, at which point the load on the specimens were removed. Side plates were affixed to the potting fixture and the entire specimen was removed from the testing machine. The failed panels were removed from the potting fixture by remelting the potting alloy.

There was an observed difference in the failure behavior between the thin (83 mm) and the wider (152 and 305 mm) test specimens. The narrow specimens demonstrated an indentation growth, perpendicular to the loading direction, that quickly spread to the edges. Failure occurred by local buckling (crippling) of the front facesheet and a global type buckling of the back facesheet. The wide specimens failed differently. Under load, there was initially no indication of damage growth. At approximately 50% of the ultimate load, the damage growth, perpendicular to the loading direction, was visible. The indentation grew slightly deeper and wider with an outward wrinkle (hump) above and below the damage. The perpendicular indentation growth appeared to arrest approximately 38 mm from the specimen centerline. The final failure on the front facesheet was precipitated by a very quick indentation propagation to the edges of the specimen with a global-type failure of the back facesheet. The failure mechanisms of the flat and curved specimens were similar.

The failure loads of all test panels were recorded using the testing machine instrumentation and plotted in terms of failure stress in figure 25. BVID can cause a significant reduction in the residual strength of a sandwich panel. The 83-mm flat panels tested in this program showed a 42% reduction in residual strength (figure 25). Plotting the failure stress against the test panel width (figure 26) for damaged panels shows the effect of panel width. The 83-mm panels do show some finite width effect, having a slightly lower ultimate stress than the wider sections. The ultimate stress of the remaining flat and curved specimens does not seem to be affected by the global geometry of the panel.

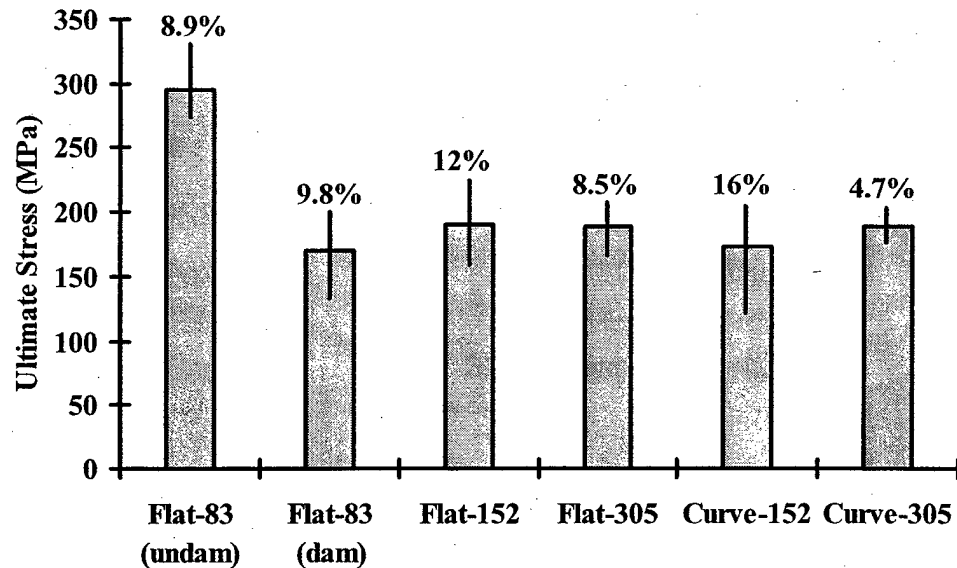


FIGURE 25. FAILURE STRESSES OF CAI PANELS

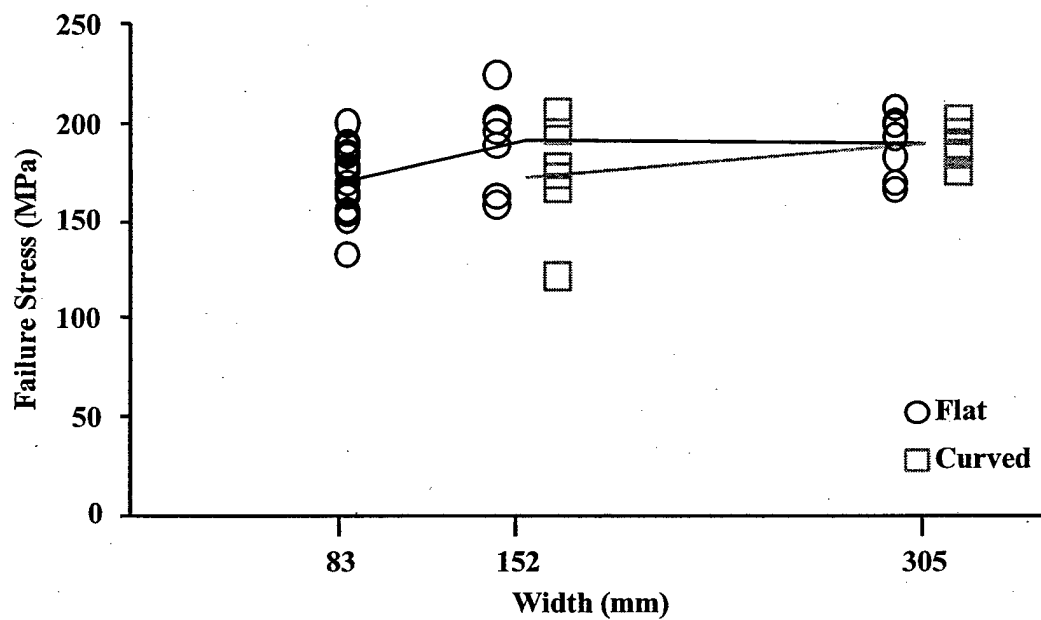


FIGURE 26. FAILURE STRESS VS SPECIMEN WIDTH FOR DAMAGED PANELS

Strain-gage data from the tests demonstrated several interesting aspects on the behavior of the panel under load. Graphs of all the strain-gage data collected can be found in reference 5.

The gage located nearest (25.4 mm from the center) to the damage area (gage no. 2) captures the indentation propagation (damage growth). This gage shows a knee in response to the loading at a

relatively low-strain level (figure 27). LIN6 [6], an algorithm that determines lines of maximum correlation, was used to establish the location of the knee. For the case shown here (figure 27), the knee locates a change in tangent modulus of approximately 28%. This knee represents the out-of-plane deformation of the facesheet in the region of gage no. 2. LIN6 was used to define the growth stress of all impacted specimens (figure 28).

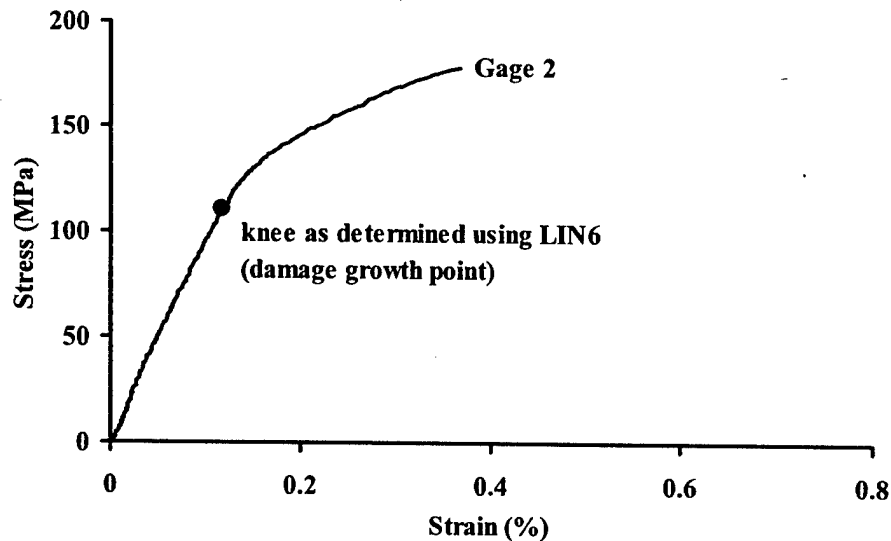


FIGURE 27. DAMAGE GROWTH—TYPICAL GAGE-2 DATA

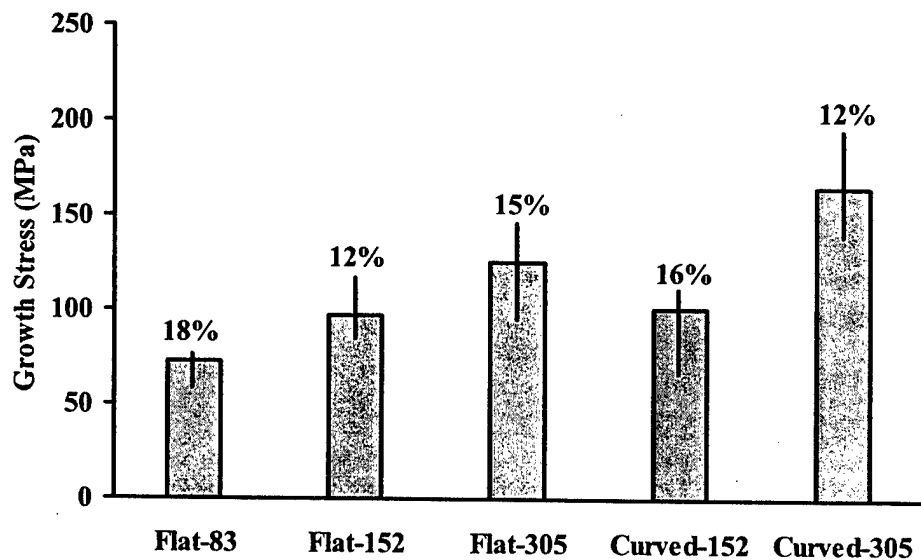


FIGURE 28. DAMAGE GROWTH STRESS

Unlike the ultimate stress, the stress at which the impact damage will grow does seem to be affected by the global geometry of the panel (figure 29). Width and curvature appear to delay the onset of damage growth.

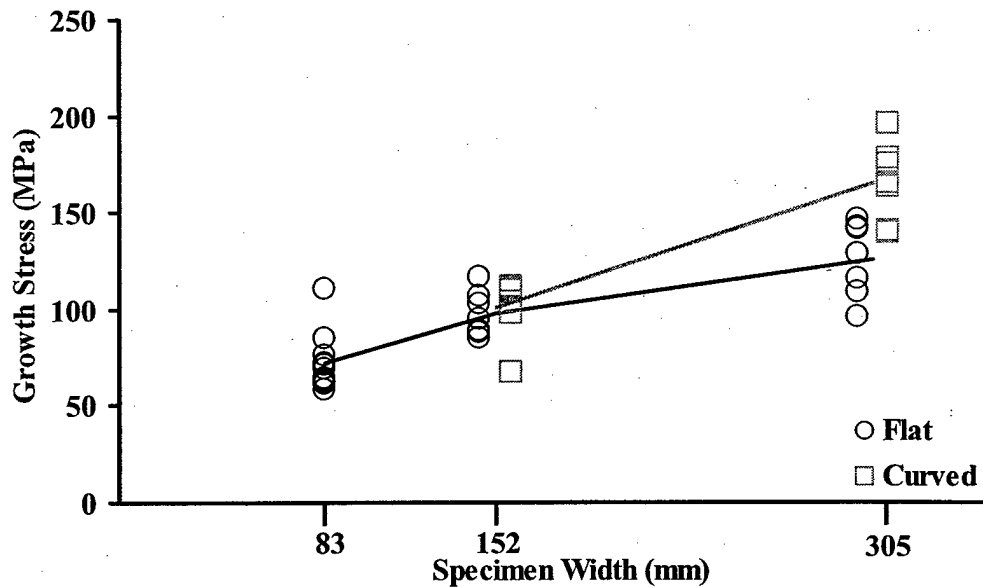


FIGURE 29. DAMAGE GROWTH STRESS VS SPECIMEN WIDTH

The damage growth arrest behavior observed during the CAI tests was also captured by the strain-gage data (figure 30). The stress-strain curves show the lateral propagation of the residual indentation at gage no. 2 location (25.4 mm from the specimen centerline). Gage no. 3 location (38.1 mm from the centerline) only records a slight response to the damage growth. This indicates that the growth was arrested at some point between gages no. 2 and 3 and agrees with the observations made during the CAI tests.

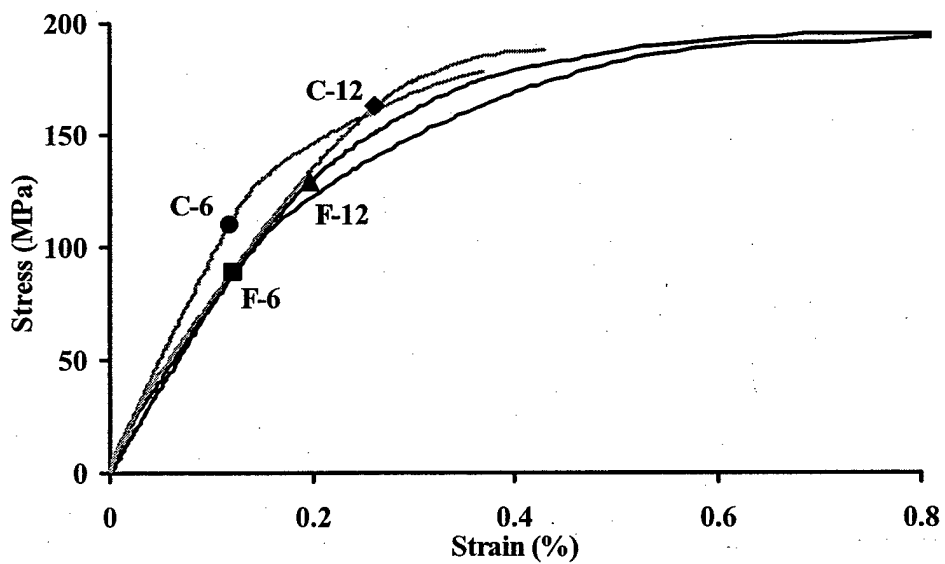


FIGURE 30. TYPICAL GAGE-2 DATA FOR DIFFERENT GEOMETRIES

4. ANALYSIS.

The main goal of the analysis is to establish a method that is capable of capturing analytically the damage growth seen in the experimentation. This analysis will shed light on the mechanisms of damage growth and the effects of global geometry.

4.1 SECTION PROPERTY ANALYSIS.

The results from the CAI study show that the growth stress for a panel in compression may be dependent upon the global geometry of that panel. For flat panels, the growth stress increases as the width increases; growth stress also increases with curvature. This suggests that the growth stress may be a function of the section properties of the panel, in particular the bending stiffness (EI). The compliance of the front facesheet, caused by the impact event, may result in a dissimilar membrane stiffness between the facesheets, and because of this, in a global bending of the panel.

To investigate the effect of global-section properties on the growth stress, a comparison of the section properties between the different CAI panels was made. All sections studied contained a region of compliant facesheet to represent the impact damage to the front facesheet (figure 31). The equations for the EI for these flat and curved panels were derived from equations 5-8.

$$\bar{c}_{flat} = t_c \left(\frac{1-\alpha+\alpha\beta}{2-\alpha+\alpha\beta} \right) \quad (5)$$

$$EI_{flat} = 2Et_f w \left(\bar{c}^2 + (1-\alpha+\alpha\beta)(t_c - \bar{c})^2 \right) \quad (6)$$

$$\bar{c}_{curved} = \frac{((2R+t_c)Sin(\theta_w) + (R+t_c)(\beta-1)Sin(\alpha\theta_w))}{((2+\alpha(\beta-1))\theta_w)} \quad (7)$$

$$\begin{aligned} EI_{curved} = & \frac{1}{2} ERt_f (2(4\bar{c}^2 + 2R^2 + 2Rt_c + t_c^2 - 2\bar{c}^2\alpha - R^2\alpha - 2Rt_c\alpha - t_c^2\alpha \\ & + (2\bar{c}^2 + (R+t_c)^2)\alpha\beta)\theta_w - 8\bar{c}(2R+t_c)Sin(\theta_w) \\ & + (2R^2 + 2Rt_c + t_c^2)Sin(2\theta_w) \\ & + 2(R+t_c)(\beta-1)(-4\bar{c} + (R+t_c)Cos(\alpha\theta_w))Sin(\alpha\theta_w)) \end{aligned} \quad (8)$$

where:

- \bar{c} : centroid of the panel
- t_c : thickness of the core
- α : damage width factor
- β : damage stiffness factor
- w : panel width
- R : radius of curvature
- θ_w : width angle of curved panel

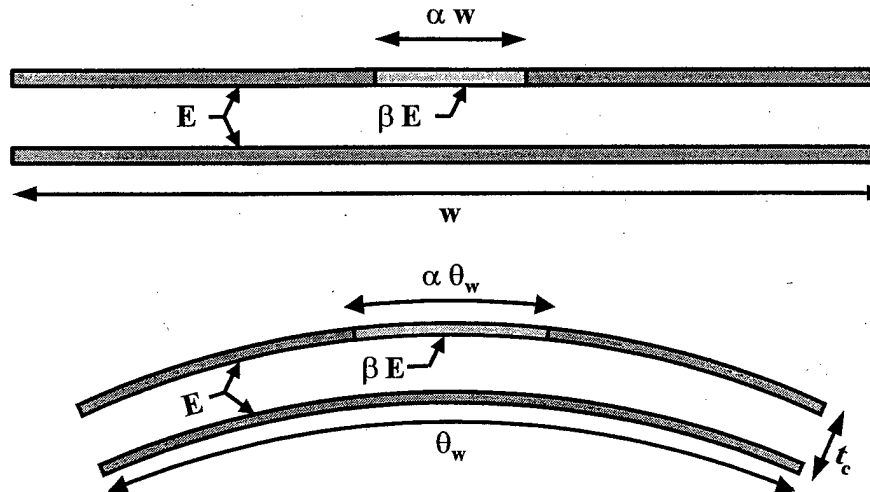


FIGURE 31. SECTION PROPERTY MODELS

The bending stiffness for each type of CAI specimen was calculated using the above equations. The typical damage region width observed in the ID specimens was approximately 51 mm. The damage region width factor α was chosen to represent this width. Damaged bending stiffness per unit width was used to compare the bending stiffness for the different widths and curvatures. The damaged bending stiffness per unit width of all panels were normalized to that of the 83-mm flat panel with a zero stiffness ($\beta=0$) damage region and plotted versus β (figure 32). Average growth stresses recorded from testing were normalized to the 83-mm flat panels and are included in the graph.

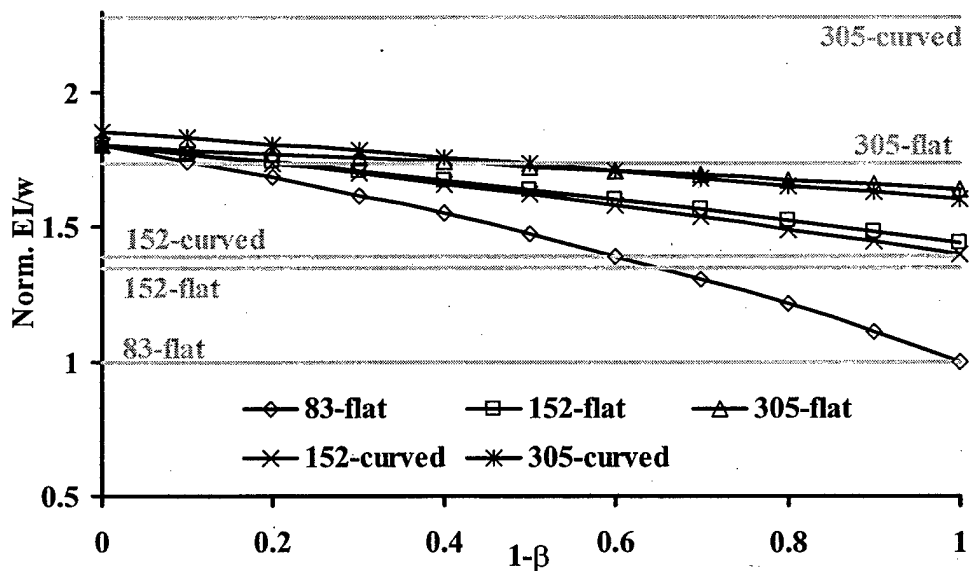


FIGURE 32. SECTION PROPERTY ANALYSIS RESULTS
(With damage growth stress test results)

This comparison between the experimental growth stress and the calculated bending stiffness shows that the damaged bending stiffness, per unit width, comes close to matching the general trend of growth stress dependence on bending stiffness; however, the magnitudes of the calculated values do not approximate the experimental data. Therefore, the damaged bending stiffness per unit width of a section through the damaged region of a panel is not useful in predicting growth stress.

4.2 FINITE ELEMENT ANALYSIS.

The effect of membrane stiffness differential and global bending was further investigated through the use of finite element modeling. This analysis used a simple model to look at the global behavior of the panel under load. Models corresponding to the five different sizes of CAI specimens were analyzed.

The finite element models of the panels were constructed with 8-noded thin-shell elements representing the facesheets and 20-noded solid elements representing the core (figure 33). The properties of the facesheets and core were similar to those of the materials used in the experimental program (equations 9 and 10).

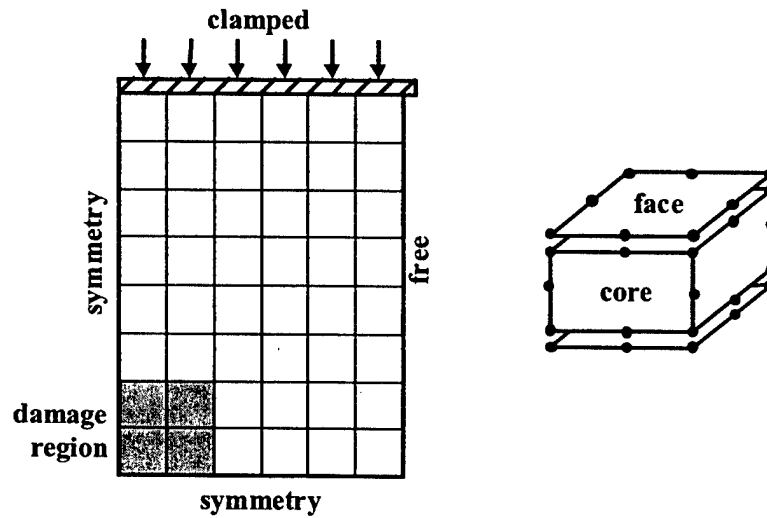


FIGURE 33. GEOMETRY OF FINITE ELEMENT MODEL

$$\begin{bmatrix} A & B \\ B & D \end{bmatrix} = \begin{bmatrix} 42.29 & 1.561 & 0 & 0 & 0 & 0 \\ 1.561 & 42.29 & 0 & 0 & 0 & 0 \\ 0 & 0 & 3.666 & 0 & 0 & 0 \\ 0 & 0 & 0 & 0.3465 & 0.03737 & 0 \\ 0 & 0 & 0 & 0.03737 & 1.678 & 0 \\ 0 & 0 & 0 & 0 & 0 & 0.08777 \end{bmatrix} \begin{bmatrix} \text{GPa} - \text{mm} & \text{GPa} - \text{mm}^2 \\ \text{GPa} - \text{mm}^2 & \text{GPa} - \text{mm}^3 \end{bmatrix} \quad (9)$$

$$[C]_{\text{CORE}} = \begin{bmatrix} 22.0 & 6.65 & 2.43 & 0 & 0 & 0 \\ 6.65 & 22.1 & 6.77 & 0 & 0 & 0 \\ 2.43 & 6.77 & 302 & 0 & 0 & 0 \\ 0 & 0 & 0 & 2.02 & 0 & 0 \\ 0 & 0 & 0 & 0 & 30.3 & 0 \\ 0 & 0 & 0 & 0 & 0 & 48.3 \end{bmatrix} \text{ kPa} \quad (10)$$

Because the problem has two planes of symmetry, only one-quarter of the panel was modeled. Appropriate boundary conditions were added to the symmetric borders. The remaining boundary conditions were similar to those of the experiments with clamped ends and free edges. The load was applied as a uniform displacement of 0.04 mm at the clamped ends of the specimen. This quantity corresponded to an average of 10,000 μ strain over the entire area of the panel. The impact damage was included as a compliant region of the facesheet. The properties of the elements in this region have a compliance factor (β) affecting all components of their stiffness matrices. This compliance factor was varied between one and zero to simulate various levels of damage. The damage region consisted of a 51- by 51-mm square in the center of the front facesheet.

The out-of-plane deflections calculated in the finite element analysis (FEA) show that the panels undergo some bending (figures 34 and 35). The average out-of-plane displacement of each type of panel is plotted versus the compliance factor (figure 36). From this graph, it is apparent that the wider and curved panels (with higher bending stiffness) experience less global bending under load. These differences are more pronounced at higher damage levels. Also, the amount of global bending is fairly small, even for the 83-mm panels. At the maximum damage level, and most compliant panel, an out-of-plane displacement of 0.8 mm represents an approximate radius of curvature of 6452 mm.

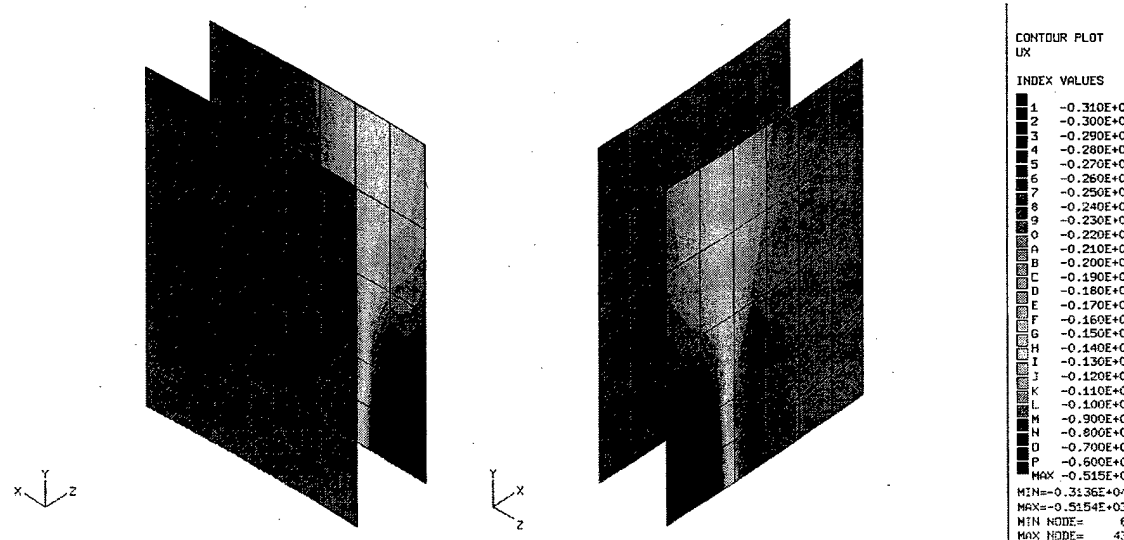


FIGURE 34. IN-PLANE LOAD (N_x) IN FRONT AND BACK FACESHEET
(Curved-152, $\beta = 10\%$)

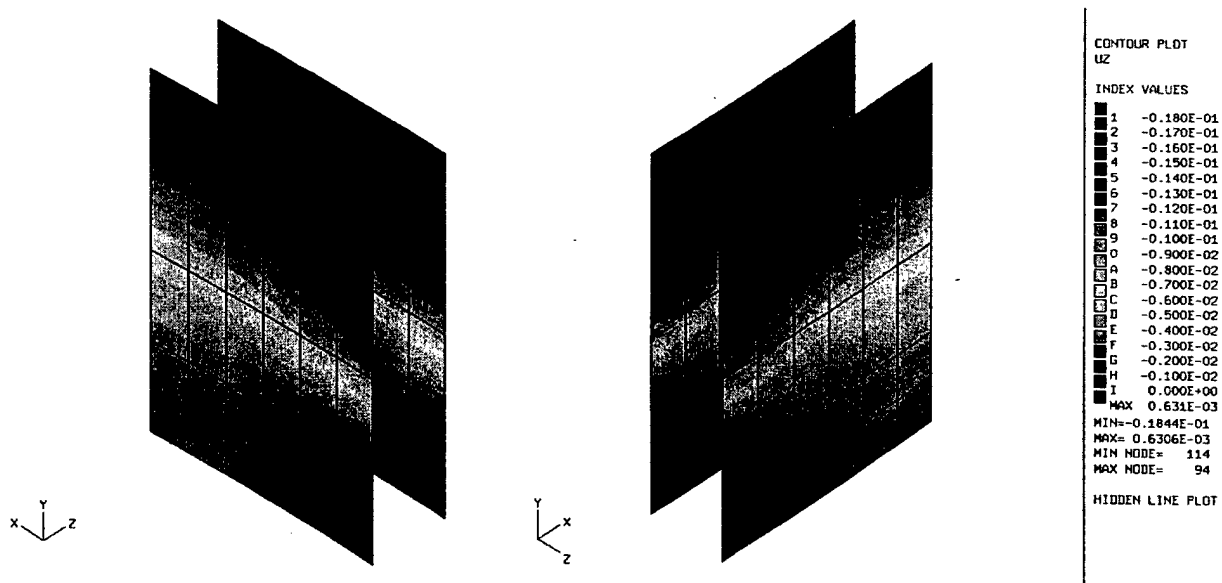


FIGURE 35. OUT-OF-PLANE DISPLACEMENTS OF FRONT AND BACK FACESHEETS (Curved-152, $\beta = 10\%$)

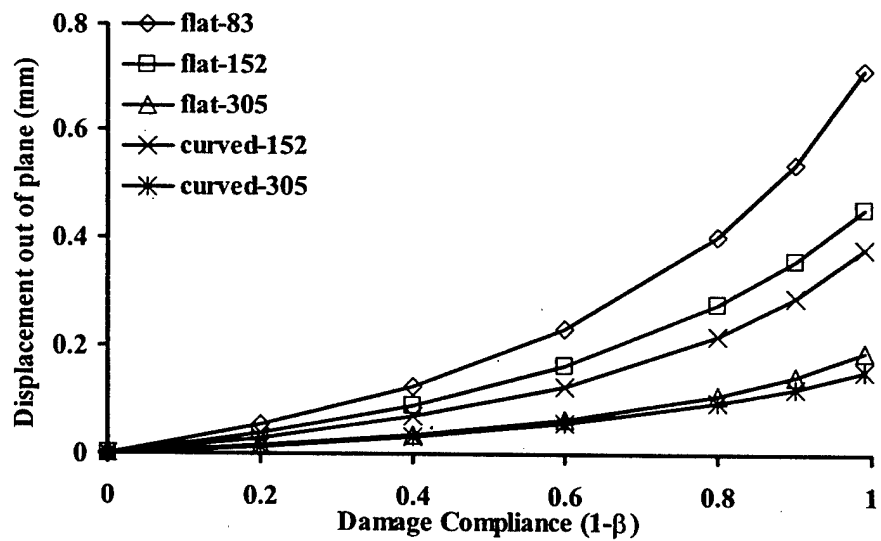


FIGURE 36. MID-PANEL DISPLACEMENT VS DAMAGED REGION COMPLIANCE

In the case where bending was occurring, a load differential between the front and back facesheet would take place. To look at this load differential, the finite element model reactions at the front and back facesheets were totaled across the width of the panel at 102 mm along the length. The ratios of the reactions versus the compliance factor (figure 37) demonstrate the overall load differential. Again, the effect of global-bending stiffness is shown with the stiffer panels having lower load differential. Among the wide and curved panels, the difference is small, even for high compliance factors.

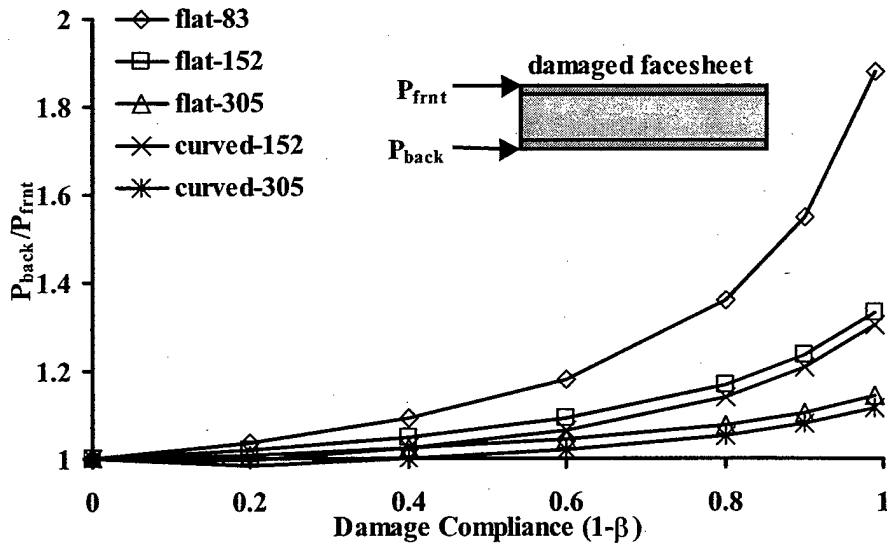


FIGURE 37. FACESHEET LOADING DIFFERENTIAL VS DAMAGED REGION COMPLIANCE

These results demonstrate several aspects of CAI behavior. At these damage levels, the specimen undergoes very little global bending as a result of loading. The testing confirmed that during compression there was no observed global bending of any panel. Strain-gage data also show little global bending. The strain-gage results for the far-field gages on the front and back facesheet show very similar slopes to failure. The damage propagation appears to be local to the front facesheet and not significantly influenced by the back facesheet.

4.3 MINGUET/TSANG MODEL (ADAPTED).

Observations of the behavior of the CAI specimens under load and the results from the simple FE analysis contributed to the selection of the next analysis method. The only model presented in the literature that is capable of predicting damage growth is the one initially proposed by Minguet [4] and later adapted by Tsang [3]. This method includes the effects of the residual indentation of the facesheet and damage to the core. This model, adapted to include the effects of facesheet damage, was used for this analysis. The following sections will detail some of the aspects of the model as proposed by Minguet and Tsang, as well as the changes made in this program.

The research presented by Tsang indicates that low-energy impact to thin-gage sandwich panels results in damage to both the core and the facesheets of the panel. The model as presented by Minguet/Tsang only includes the effects of damage to the core. Governing equations were developed to include both core and facesheet damage. The governing equations used by Tsang were derived from Marguerre equations of an initially deformed plate under lateral loads. These equations were adapted to include the effects of a local compliance increase, due to impact damage, in order to represent the damage to the facesheet such as delamination, matrix cracking, or fiber breakage. Solutions to these equations were sought in the form of expanded Fourier series. The following sections detail the derivation of the governing equations, the expansion of the variables, substitution into the governing equations, solution method, and the analysis results.

4.3.1 Governing Equations.

Consider a thin, deformed plate approximating a flat plate. The middle surface of this plate is defined by $\xi(x, y)$, which defines the local residual indentation of the panel caused by the impact. The position vector of a point located on the mid-plane of the undeformed surface is represented by:

$$\mathbf{r}_0 = xi + yj(z + \xi)k \quad (11)$$

The Kirchoff's hypothesis provides the following deformations of a plate

$$\begin{aligned} u &= u^0 - zw_{,x} \\ v &= v^0 - zw_{,y} \\ w &= w^0, \end{aligned} \quad (12)$$

where the 0 superscript refers to the deflections of the midplane.

The position vector of a point at the mid-plane of the deformed panel is given by

$$\mathbf{r} = (x + u) i + (y + v) j + (z + \xi + w) k \quad (13)$$

Equation 13 is incorporated into equation 14

$$\mathbf{r} = (x + u^0 - zw_{,x}) i + (y + v^0 - zw_{,y}) j + (z + \xi + w^0) k \quad (14)$$

To determine the strain, the differential linear element is calculated:

$$d\mathbf{r}_0 = dx i + dy j + [(z + \xi)_{,x} dx + (z + \xi)_{,y} dy] k \quad (15)$$

$$\begin{aligned} d\mathbf{r} = & \{ [1 + u^0_{,x} - (zw^0_{,x})_{,x}] dx + [u^0_{,y} - (zw^0_{,x})_{,y}] dy \} i \\ & + \{ [v^0_{,x} - (zw^0_{,y})_{,x}] dx + [1 + v^0_{,y} - (zw^0_{,y})_{,y}] dy \} j \\ & + [(z + \xi + w^0)_{,x} dx + (z + \xi + w^0)_{,y} dy] k \end{aligned} \quad (16)$$

$$\begin{aligned} ds_0^2 &= d\mathbf{r}_0 \cdot d\mathbf{r}_0 \\ &= \{1 + [(z + \xi)_{,x}]^2\} dx^2 \\ &\quad + 2(z + \xi)_{,x} (z + \xi)_{,y} dx dy \\ &\quad + \{1 + [(z + \xi)_{,y}]^2\} dy^2 \end{aligned} \quad (17)$$

$$\begin{aligned}
ds^2 = & \left\{ [1+u^o_x - (zw^o_x)_x]^2 + [v^o_x - (zw^o_y)_x]^2 + (z+\xi+w^o)_x^2 \right\} dx^2 \\
& + 2 \left\{ [1+u^o_x - (zw^o_x)_x] [u^o_y - (zw^o_x)_y] \right. \\
& \left. + [v^o_x - (zw^o_y)_x] [1+v^o_y - (zw^o_y)_y] \right\} dx dy \\
& + \left\{ [u^o_y - (zw^o_x)_y]^2 + [1+v^o_y - (zw^o_y)_y]^2 + (z+\xi+w^o)_y^2 \right\} dy^2
\end{aligned} \tag{18}$$

Strain can be determined by

$$ds^2 - ds_0^2 = 2\epsilon_{ij} dx_i dx_j \tag{19}$$

For plates, equation 19 becomes

$$ds^2 - ds_0^2 = 2(\epsilon_{xx} dx^2 + 2\epsilon_{xy} dx dy + \epsilon_{yy} dy^2) \tag{20}$$

Inserting equations 18 and 19 into equation 20 and dropping the higher order terms (products of two derivatives) and any derivative of z (the plate is of constant thickness) results in:

$$\begin{aligned}
\epsilon_{xx} &= u^o_{,x} + \frac{1}{2} (u^o_{,x}^2 + v^o_{,x}^2 + w^o_{,x}^2) + \xi_{,x} w^o_{,x} - zw^o_{,xx} \\
\epsilon_{yy} &= v^o_{,y} + \frac{1}{2} (v^o_{,y}^2 + u^o_{,y}^2 + w^o_{,y}^2) + \xi_{,y} w^o_{,y} - zw^o_{,yy} \\
\epsilon_{xy} &= u^o_{,y} + u^o_{,x} u^o_{,y} + v^o_{,x} v^o_{,y} + \xi_{,x} w^o_{,y} + \xi_{,y} w^o_{,x} + w^o_{,x} w^o_{,y} - 2zw^o_{,xy}
\end{aligned} \tag{21}$$

For an almost flat plate, the in-plane strain terms, such as $u^o_{,x}$ (and similar) are small in comparison to the out-of-plane terms containing w . Higher orders of these terms are dropped (such as $u^o_{,x} u^o_{,y}$). The strain terms become

$$\begin{aligned}
\epsilon_{xx} &= u^o_{,x} + \frac{1}{2} (w^o_{,x}^2) + \xi_{,x} w^o_{,x} - zw^o_{,xx} \\
\epsilon_{yy} &= v^o_{,y} + \frac{1}{2} (w^o_{,y}^2) + \xi_{,y} w^o_{,y} - zw^o_{,yy} \\
\epsilon_{xy} &= u^o_{,y} + v^o_{,x} + \xi_{,x} w^o_{,y} + \xi_{,y} w^o_{,x} + w^o_{,x} w^o_{,y} - 2zw^o_{,xy}
\end{aligned} \tag{22}$$

The strain (potential) energy can be written as

$$U = \iiint_{Vol} \sigma_{ij} \epsilon_{ij} dz dy dx \tag{23}$$

Or, for this deformed plate with constant thickness

$$U = \iint_A \int_{-\frac{t}{2}}^{\frac{t}{2}} (\sigma_{xx} \epsilon_{xx} + \sigma_{xy} \epsilon_{xy} + \sigma_{yy} \epsilon_{yy}) dz dy dx \quad (24)$$

Insert equation 22 into equation 24 results in

$$U = \frac{1}{2} \iint_A \int_{-\frac{t}{2}}^{\frac{t}{2}} (\epsilon_{xx}'' \sigma_{xx} + \epsilon_{xy}'' \sigma_{xy} + \epsilon_{yy}'' \sigma_{yy}) dz dy dx \quad (25)$$

$$- \frac{1}{2} \iint_A \int_{-\frac{t}{2}}^{\frac{t}{2}} (w_{,xx}^o \sigma_{xx} + 2w_{,xy}^o \sigma_{xy} + w_{,yy}^o \sigma_{yy}) dz dy dx$$

Where the first term of equation 25 represents the strain energy due to the membrane strains and the second term represents the strain energy due to the bending strain, where

$$\epsilon_{xx}'' = u_{,x}^o + \frac{1}{2} (w_{,x}^o)^2 + \xi_{,x} w_{,x}^o, \quad (26)$$

$$\epsilon_{yy}'' = v_{,y}^o + \frac{1}{2} (w_{,y}^o)^2 + \xi_{,y} w_{,y}^o,$$

$$\epsilon_{xy}'' = u_{,y}^o + v_{,x}^o + \xi_{,x} w_{,y}^o + \xi_{,y} w_{,x}^o + w_{,x}^o w_{,y}^o,$$

Using nomenclature from Classical Laminated Plate Theory (CLPT)

$$N_{xx} = \int_{-\frac{t}{2}}^{\frac{t}{2}} \sigma_{xx} dz \quad \text{similar for } N_{yy}, N_{xy} \quad (27)$$

$$M_{xx} = \int_{-\frac{t}{2}}^{\frac{t}{2}} \sigma_{xx} z dz \quad \text{similar for } M_{yy}, M_{xy}$$

Strain (potential) energy of the deformed plate becomes

$$U = \frac{1}{2} \iint_A (\epsilon_{xx}'' N_{xx} + \epsilon_{xy}'' N_{xy} + \epsilon_{yy}'' N_{yy}) dx dy \quad (28)$$

$$- \frac{1}{2} \iint_A (w_{,xx}^o M_{xx} + 2w_{,xy}^o M_{xy} + w_{,yy}^o M_{yy}) dx dy$$

For simplicity, the edges of the plate are considered to be simply supported, thus, the potential energy of the external forces goes to zero at the boundary. While this does not match the clamped-free boundary conditions found in the experimental program, the high-bending stiffness of the sandwich panel does cause it to behave similar to a simply supported plate in that the global buckling is at a higher energy level. Specimens with lower bending stiffness (such as sandwich panels with thin core) may show global buckling as a lower energy mode, making this assumption invalid for such panels. The external potential energy (of the foundation or core) can be written as

$$V = \iint_A q w dy dx \quad (29)$$

Where q is the out-of-plane stress created by the foundation (core). Total energy then becomes

$$\begin{aligned} \Pi &= U - V \\ &= \frac{1}{2} \iint_A (\varepsilon_{xx}^m N_{xx} + \varepsilon_{xy}^m N_{xy} + \varepsilon_{yy}^m N_{yy}) dx dy \\ &\quad - \frac{1}{2} \iint_A (w_{,xx}^o M_{xx} + 2w_{,xy}^o M_{xy} + w_{,yy}^o M_{yy}) dx dy \\ &\quad - \iint_A q w dy dx \end{aligned} \quad (30)$$

To uncouple the bending strain energy and the membrane strain energy, the laminate is assumed to be symmetric with orthotropic plies, where

$$B_{ij} = A_{16} = A_{26} = D_{16} = D_{26} = 0 \quad (31)$$

From CLPT:

$$\begin{aligned} M_{xx} &= -D_{11} w_{,xx} - D_{12} w_{,yy} \\ M_{yy} &= -D_{12} w_{,xx} - D_{22} w_{,yy} \\ M_{xy} &= -2D_{66} w_{,xy} \end{aligned} \quad (32)$$

In this case, the effects of a local loss in stiffness around the damage region are of interest. For this purpose, two stiffness factors are introduced, one affecting the membrane stiffness of the facesheet ($\alpha(x, y)$), the other affecting the bending stiffness of the facesheet ($\beta(x, y)$). Together, these factors represent the facesheet material damage (regional delamination, matrix cracking, and fiber breakage).

$$\begin{aligned} A_{ij}^{dam} &= \alpha A_{ij}^{und} \\ D_{ij}^{dam} &= \beta D_{ij}^{und} \end{aligned} \quad (33)$$

Inserting these equations into the total energy equation:

$$\begin{aligned}\Pi = & \frac{1}{2} \iint_{\text{Area}} (\varepsilon_{xx}^m N_{xx} + \varepsilon_{xy}^m N_{xy} + \varepsilon_{yy}^m N_{yy}) dx dy \\ & + \frac{1}{2} \iint_{\text{Area}} \beta (D_{11} w^o,_{xx}^2 + D_{22} w^o,_{yy}^2 + 2D_{12} w^o,_{xx} w^o,_{yy} + 4D_{66} w^o,_{xy}^2) dx dy \\ & - \iint_{\text{Area}} q w dy dx\end{aligned}\quad (34)$$

First minimizing the energy equation for minimum potential energy with respect to u^o and v^o :

$$\begin{aligned}N_{xx, x} + N_{xy, y} &= 0 \\ N_{xy, x} + N_{yy, y} &= 0\end{aligned}\quad (35)$$

These two equations can be satisfied with the Airy stress functions, where:

$$\begin{aligned}N_{xx} &= t\sigma_{xx} = t\Phi_{yy} \\ N_{yy} &= t\sigma_{yy} = t\Phi_{xx} \\ N_{xy} &= t\sigma_{xy} = -t\Phi_{xy}\end{aligned}\quad (36)$$

Minimizing the total potential energy equation with respect to w leaves:

$$\begin{aligned}& \beta (D_{11} w,_{xxxx} + 2D_{12} w,_{xxyy} + D_{22} w,_{yyyy} + 4D_{66} w,_{xxyy}) \\ & + \beta,_{x} (2D_{11} w,_{xxx} + 2D_{12} w,_{xyy} + 4D_{66} w,_{xyy}) \\ & + \beta,_{y} (2D_{12} w,_{xyy} + 2D_{22} w,_{yyy} + 4D_{66} w,_{xxy}) + \beta,_{xx} (D_{11} w,_{xx} + D_{12} w,_{yy}) \\ & + \beta,_{yy} (D_{12} w,_{xx} + D_{22} w,_{yy}) + \beta,_{xy} (4D_{66} w,_{xy}) \\ & = q + t\Phi_{yy} (w + \xi),_{xx} - 2t\Phi_{xy} (w + \xi),_{xy} + t\Phi_{yy} (w + \xi),_{xx}\end{aligned}\quad (37)$$

Introducing the condition of compatibility for a plate:

$$\begin{aligned}\varepsilon_{xx}^m,_{yy} + \varepsilon_{yy}^m,_{xx} - \varepsilon_{xy}^m,_{xy} &= w^o,_{xy}^2 - w^o,_{xx} w^o,_{yy} + 2\xi,_{xy} w^o,_{xy} \\ & - \xi,_{xx} w^o,_{yy} - \xi,_{yy} w^o,_{xx}\end{aligned}\quad (38)$$

For a symmetric laminate (with $A_{16} = A_{26} = 0$):

$$\begin{Bmatrix} N_{xx} \\ N_{yy} \\ N_{xy} \end{Bmatrix} = \alpha \begin{bmatrix} A_{11} & A_{12} & - \\ A_{12} & A_{22} & - \\ - & - & A_{66} \end{bmatrix} \begin{Bmatrix} \varepsilon_{xx}^m \\ \varepsilon_{yy}^m \\ \varepsilon_{xy}^m \end{Bmatrix}\quad (39)$$

Inverting the equation:

$$\begin{Bmatrix} \varepsilon_{xx}^m \\ \varepsilon_{yy}^m \\ \varepsilon_{xy}^m \end{Bmatrix} = \alpha^* \begin{bmatrix} A_{11}^* & A_{12}^* & - \\ A_{12}^* & A_{22}^* & - \\ - & - & A_{66}^* \end{bmatrix} \begin{Bmatrix} N_{xx} \\ N_{yy} \\ N_{xy} \end{Bmatrix} \quad (40)$$

where:

$$\alpha^* = \alpha^{-1} \quad (41)$$

Inserting equation 40 into the compatibility equation 38:

$$\begin{aligned} & \alpha^* (2A_{12}^* \Phi_{,xyy} + A_{22}^* \Phi_{,xxx} + A_{11}^* \Phi_{,yyy} - A_{66}^* \Phi_{,xxy}) \\ & + \alpha^* ,_x (-A_{66}^* \Phi_{,xy} + 2A_{12}^* \Phi_{,xyy} + 2A_{22}^* \Phi_{,xxx}) \\ & + \alpha^* ,_y (-A_{66}^* \Phi_{,xy} + 2A_{11}^* \Phi_{,yyy} + 2A_{12}^* \Phi_{,xxy}) \\ & + \alpha^* ,_{xx} (A_{12}^* \Phi_{,yy} + A_{22}^* \Phi_{,xx}) + \alpha^* ,_{yy} (A_{11}^* \Phi_{,yy} + A_{12}^* \Phi_{,xx}) \\ & + \alpha^* ,_{xy} (-A_{66}^* \Phi_{,xy}) \\ & = \frac{1}{t} (w^o_{,xy}^2 - w^o_{,xx} w^o_{,yy} + 2\xi_{,xy} w^o_{,xy} - \xi_{,xx} w^o_{,yy} - \xi_{,yy} w^o_{,xx}) \end{aligned} \quad (42)$$

The two governing equations are 37 and 42. In the case where there is no localized loss in ply membrane or bending stiffness due to the impact event ($\alpha^* = \beta = 1$), the governing equations are equal to those derived by Tsang.

4.3.2 Equation Expansion.

The functions of the governing equations were expanded into Fourier series approximations. This series was chosen so that the boundary conditions of the governing equations are satisfied, and a solution could be reached. Because the problem is symmetric about the x and y axis, the variables were expanded by using a sin series with only the odd modes. The variables were expanded by using a cos series with only the even modes as noted below.

The out-of-plane deformation of the mid-plane of the plate under load, one of the two unknowns, is approximated by:

$$w(x, y) = \sum_i \sum_j w_{ij} \sin\left(\frac{i\pi x}{a}\right) \sin\left(\frac{j\pi y}{b}\right) \quad i, j = 1, 3, 5, \dots \quad (43)$$

The Airy stress function, the second unknown, is approximated by equation 44. The term representing the far-field stress is included on the right-hand side of the expansion.

$$\Phi(x,y) = \sum_k \sum_l f_{kl} \cos\left(\frac{k\pi x}{a}\right) \cos\left(\frac{l\pi y}{b}\right) + \bar{\sigma}_{yy} \frac{x^2}{2} \quad i,j=0,2,4,\dots \quad (44)$$

The remaining variables are dependent upon the assumptions made about the initial impact damage to the facesheet and core as well as the behavior under load. The damage model includes the effects of the residual indentation of the facesheet, the impact damage to the facesheet, the damaged core, and the disbond in the adhesive layer between the facesheet and the core as shown in figure 38.

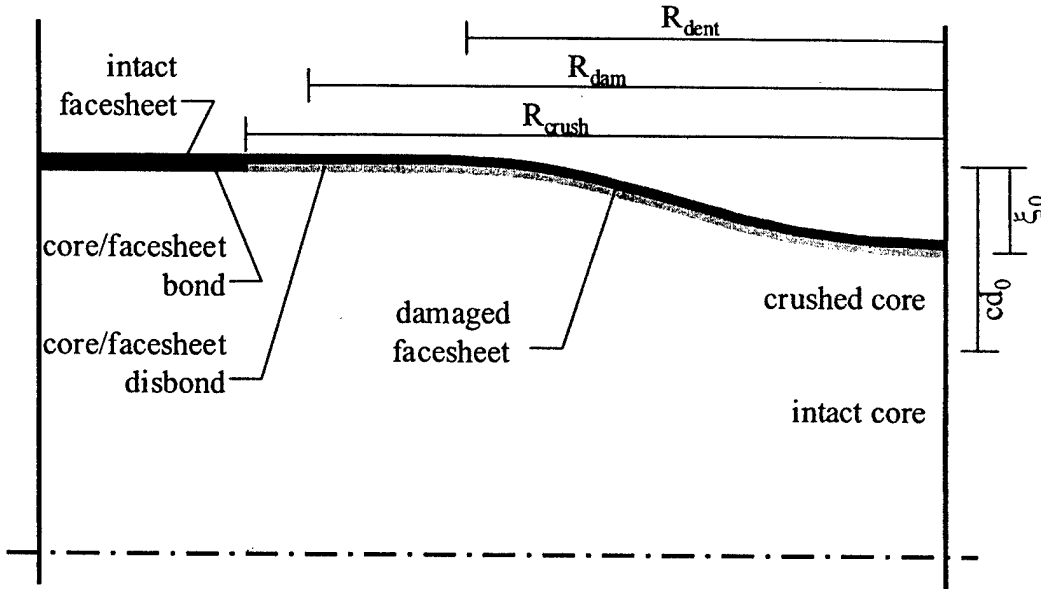


FIGURE 38. COMPONENT OF DAMAGE IN THE DAMAGED REGION

The membrane and bending stiffness factors are also approximated by Fourier series:

$$\alpha^*(x,y) = 1 + \sum_i \sum_j \alpha_{ij}^* \cos\left(\frac{i\pi x}{a}\right) \cos\left(\frac{j\pi y}{b}\right) \quad i,j=0,2,4 \quad (45)$$

$$\beta(x,y) = 1 + \sum_i \sum_j B_{ij} \cos\left(\frac{i\pi x}{a}\right) \cos\left(\frac{j\pi y}{b}\right) \quad i,j=0,2,4,\dots$$

The initial function describing the membrane stiffness factor (α^*) is assumed to be:

$$\alpha^*(x,y) = \begin{cases} \alpha_0^* \cos^2\left[\frac{\pi}{2} \left(\frac{x-\frac{a}{2}}{R_{dam,x}} \right)\right] \cos^2\left[\frac{\pi}{2} \left(\frac{y-\frac{b}{2}}{R_{dam,y}} \right)\right] & \text{for } \frac{(x-\frac{a}{2})^2}{(R_{dam,x})^2} + \frac{(y-\frac{b}{2})^2}{(R_{dam,y})^2} \leq 1.0 \\ 0 & \text{for all else} \end{cases} \quad (46)$$

The expansion for the bending stiffness factor (β) is similar. These functions result in a elliptical damage region of varying stiffness (figure 39).

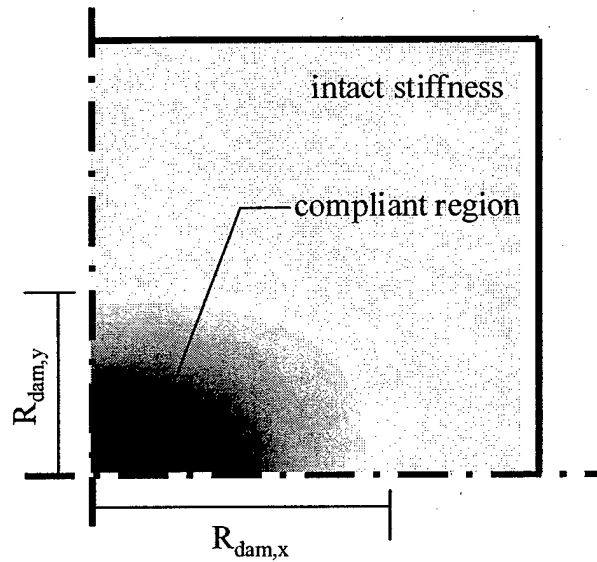


FIGURE 39. REGIONAL FACESHEET COMPLIANCE (α, β)

The initial deformed shape of the panel prior to loading is also expanded into a double Fourier series. The effects of the plate curvature are included in this approximation. The curvature of the plate can be approximated by $w_{xx} = \kappa_x$ for larger curvatures. This curvature will only show up in the terms with two derivatives in x . A negative curvature is one with the damaged facesheet on the convex side of the curve. The curvature of the facesheet is included on the right-hand side of the approximation.

$$\xi(x, y) = \sum_i \sum_j \xi_{ij} \sin \frac{i\pi x}{a} \sin \frac{j\pi y}{b} + \kappa_x \frac{(x-a/2)^2}{2} \quad (47)$$

The function that describes the initial shape of the indented panel is assumed to be

$$\xi(x, y) = \begin{cases} \xi_0 \cos^8 \left[\frac{\pi}{2} \left(\frac{x-a}{R_{dent,x}} \right) \right] \cos^8 \left[\frac{\pi}{2} \left(\frac{y-b}{R_{dent,y}} \right) \right] & \text{for } \frac{(x-a)^2}{(R_{dent,x})^2} + \frac{(y-b)^2}{(R_{dent,y})^2} \leq 1.0 \\ 0 & \text{for all else} \end{cases} \quad (48)$$

This shape was determined from the measurements made in the damage characterization section of the program (section 3.3). This results in the shape shown in figure 40.

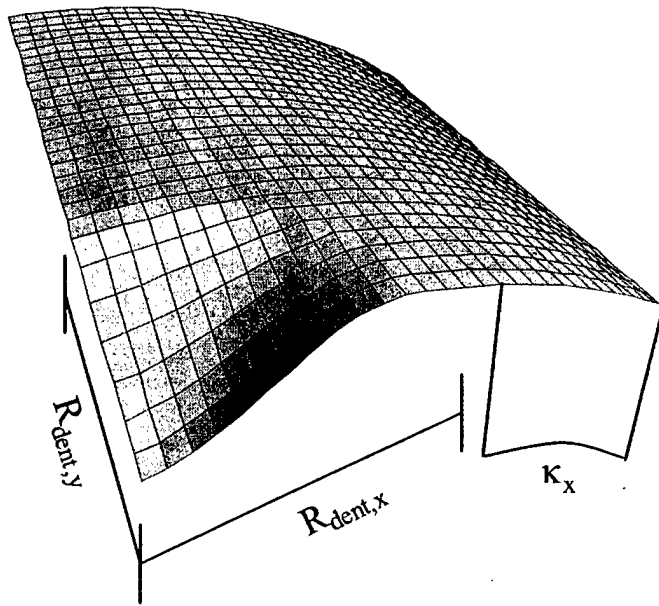


FIGURE 40. INITIAL SHAPE OF FACESHEET

The contribution of the core stiffness is shown on the right-hand side of the equilibrium in equation 37. This term has several individual components (equation 49). An orthotropic solid approximates the honeycomb core. Its contribution to the equilibrium equation is similar to the Pasternak two-parameter model originally developed for the analysis of soil-foundation interactions [7]. The shear component of the Pasternak model has been replaced with two terms representing the directional shear stiffness of the orthotropic core. The final term represents the complementary core stress and is used to impose the effects of the damaged core region and the nonlinear stress-strain curve of the core in compression.

$$q(x, y) = k_{zz} w - k_{xz} w_{,xx} - k_{yz} w_{,yy} + q^c \quad (49)$$

The complementary core stress is also approximated by a series

$$q^c(x, y) = \sum_i \sum_j q_{ij}^c \sin\left(\frac{i\pi x}{a}\right) \sin\left(\frac{j\pi y}{b}\right) \quad i, j = 1, 3, 5, \dots \quad (50)$$

The discrete values of the complementary core stress are functions of the nonlinear stress strain curve of the core material and the extent of the damage to the core. The intact core is assumed to have a nonlinear stress-strain curve in compression similar to that observed in the core properties testing (figure 41). This is modeled as a linear stiffness region up to the ultimate stress. Further displacement results in a constant plateau stress. The crushed core is assumed to have lost any shear stiffness. The stiffness of the core in tension is assumed to be linear with no ultimate stress.

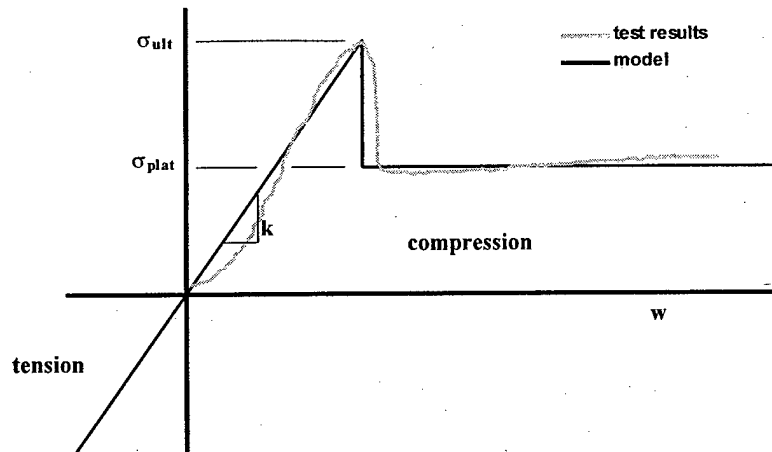


FIGURE 41. SIMPLIFIED STRESS-STRAIN CURVE OF INTACT CORE

The core behaves differently within the region of impact (figure 42). In this area, the cell walls of the core have already been crushed during the impact event. The damaged core is assumed to have lost any shear stiffness. In compression, the out-of-plane stiffness of the crushed core is zero until the deflection of the facesheet is large enough to be affected by the intact core below the crushed region. At this deflection, the core has an out-of-plane stiffness suitable for the damaged core (k_d). In the damage region, the core stress reaches a plateau stress. Any additional out-of-plane displacement will result in only the maximum plateau stress. In tension, the out-of-plane stiffness of the crushed core is also assumed to be zero until the positive deflections of the facesheet are large enough to re-tension the walls of the crushed core. This occurs when the positive deflection of the facesheet is larger than the residual indentation left after impact. Disbond in the adhesive layer between the facesheet and the core appeared to be present in the experimental panels. Such a disbond would prevent any positive load transfer between the facesheet and the damaged core. An option to include the effects of this disbond allows for this behavior.

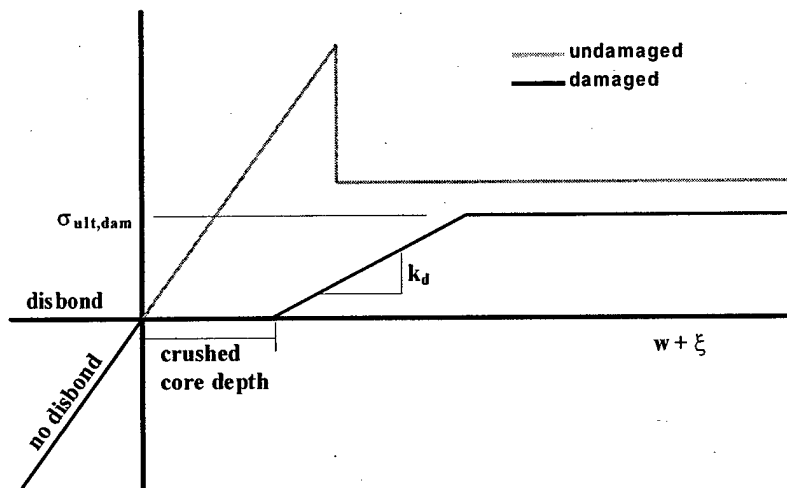


FIGURE 42. DAMAGED CORE STRESS-STRAIN CURVE

This nonlinear behavior, dependent upon location, is included in the analysis through the use of a complementary core any stress (equation 51). The complementary core stress is calculated as the difference between the stress according to the criteria described above and the elastic stress in the core.

$$q^c = q^{criteria} - q^{elastic} \quad (51)$$

There are seven criteria used to determine the complementary core stresses:

1. If the sample location is outside the damaged region and the elastic core stress is below the ultimate stress of the core material:

$$q^{criteria} = q^{elastic} \quad (52)$$

2. If the sample location is outside the damaged region and the elastic core stress is above the ultimate stress of the core material:

$$q^{criteria} = \sigma^{plat} \quad (53)$$

3. If the sample location is inside the damaged region and the negative deflection of the facesheet is less than the crushed core depth:

$$q^{criteria} = 0 \quad (54)$$

4. If the sample location is inside the damaged region and the negative deflection of the facesheet is greater than the crushed core depth and the core stress is less than the ultimate damaged stress:

$$q^{criteria} = k_{zz}^{dam} w \quad (55)$$

5. If the sample location is inside the damaged region and the negative deflection of the facesheet is greater than the crushed core depth and the core stress is greater than the ultimate damaged stress:

$$q^{criteria} = q^{ult,dam} \quad (56)$$

6. If the sample location is inside the damaged region and the positive deflection of the facesheet is greater than the residual indentation depth and there is no disbond between the facesheet and the core:

$$q^{criteria} = k_{zz} w \quad (57)$$

7. If the sample location is inside the damaged region and the positive deflection of the facesheet is greater than the residual indentation depth and there is disbond between the facesheet and the core:

$$q^{criteria} = 0 \quad (58)$$

While the discrete values of the complementary core stress q^c , the membrane and bending stiffness factors of the facesheet (α^*, β) and the initial shape of the indented facesheet (ξ) are defined by the above functions, the modal amplitudes of their corresponding expanded series are required for the substitution into the governing equations. In the case of an expansion with i modes in the x direction and j modes in the y direction, there exists $i \times j$ unknown modal amplitudes. To solve these modal amplitudes, an equal number of discrete values are required. These discrete values can be determined by sampling the known function at specific locations. Writing the expansion for the initial shape of the panel (ξ) in matrix form (with $k \times l$ sampling points):

$$\begin{Bmatrix} \xi(x_1, y_1) \\ \xi(x_1, y_2) \\ \vdots \\ \xi(x_k, y_l) \end{Bmatrix} = \begin{bmatrix} \sin \frac{\pi x_1}{a} \sin \frac{\pi y_1}{b} & \sin \frac{\pi x_1}{a} \sin \frac{3\pi y_1}{b} & \dots & \sin \frac{i\pi x_1}{a} \sin \frac{j\pi y_1}{b} \\ \sin \frac{\pi x_1}{a} \sin \frac{\pi y_2}{b} & \sin \frac{\pi x_1}{a} \sin \frac{3\pi y_2}{b} & \dots & \sin \frac{i\pi x_1}{a} \sin \frac{j\pi y_2}{b} \\ \vdots & \vdots & \ddots & \vdots \\ \sin \frac{\pi x_k}{a} \sin \frac{\pi y_l}{b} & \sin \frac{\pi x_k}{a} \sin \frac{3\pi y_l}{b} & \dots & \sin \frac{i\pi x_k}{a} \sin \frac{j\pi y_l}{b} \end{bmatrix} \begin{Bmatrix} \xi_{11} \\ \xi_{13} \\ \vdots \\ \xi_{ij} \end{Bmatrix} \quad (59)$$

The matrix relating the values for the complementary core stress (q^c) is the same as that shown above. The matrix relating the values of the membrane and bending stiffness factors (α^*, β) is similar:

$$\begin{Bmatrix} \alpha^*(x_1, y_1) \\ \alpha^*(x_1, y_2) \\ \vdots \\ \alpha^*(x_k, y_l) \end{Bmatrix} = \begin{bmatrix} 1 & \cos \frac{2\pi y_1}{b} & \dots & \cos \frac{i\pi x_1}{a} \cos \frac{j\pi y_1}{b} \\ 1 & \cos \frac{2\pi y_2}{b} & \dots & \cos \frac{i\pi x_1}{a} \cos \frac{j\pi y_2}{b} \\ \vdots & \vdots & \ddots & \vdots \\ 1 & \cos \frac{2\pi y_l}{b} & \dots & \cos \frac{i\pi x_k}{a} \cos \frac{j\pi y_l}{b} \end{bmatrix} \begin{Bmatrix} \alpha_{00}^* \\ \alpha_{02}^* \\ \vdots \\ \alpha_{ij}^* \end{Bmatrix} \quad (60)$$

The matrix that relates the discrete values to the modal amplitudes is referred to as the Fourier transformation matrix. To solve the modal amplitudes, the number of sampling points must equal the number of modes in each direction ($i = k$ & $j = l$), resulting in a square transformation matrix. To avoid getting a singular transformation matrix, care must be taken so as not to choose a sampling point that coincides with a series modal point (equation 61). Due to symmetry, only one-quarter of the panel is sampled (figure 43).

$$x = \frac{(2i-1)a}{4n} \quad (61)$$

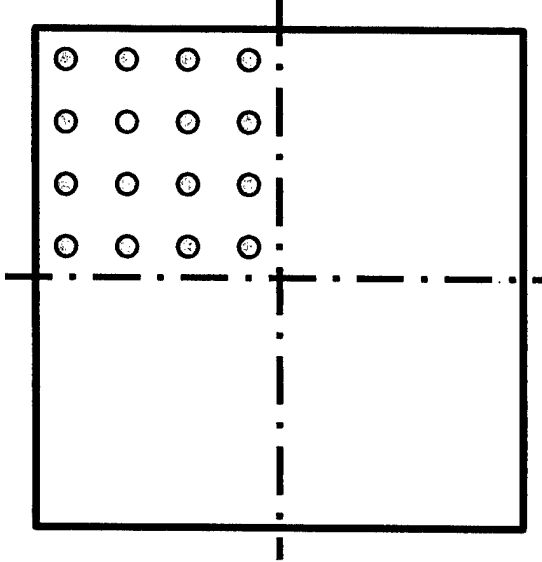


FIGURE 43. 4 x 4 SAMPLING POINTS

A lower/upper triangular (LU) decomposition is used to solve the set of $i \times j$ equations for the modal amplitudes [8]. This method allows for flexibility in writing the discrete functions describing the initial shape of the facesheet, the facesheet stiffness factors, and the complementary core stress.

This procedure is used at the beginning of the analysis to determine the modal amplitudes of the initial shape of the facesheet (ξ) as well as the membrane and bending stiffness factors of the facesheet (α^*, β). At each iteration, the modal amplitudes of the complementary core stress (q^c) are updated in the same manner.

These series were selected to successfully solve the governing equations. They do not, however, accurately represent the boundary conditions of the experimentation. The deformation series (w) satisfies the boundary conditions for a simply supported plate ($w = 0$ at $x = 0, a$ and $y = 0, b$). The tested panels were clamped on the ends and free at the edges. The Airy stress series (Φ) also differs from the boundary conditions, allowing stress at the edges of the panel ($x = 0, a$). The boundary conditions as tested were $\Phi_{,xx} = 0$ at $x = 0, a$ and $\Phi_{,yy} = \sigma_{,yy}$ at $y = 0, b$. This is not required by the proposed series. The solution away from the edges is probably accurate, as the edge begins to affect the results, the solutions will be different from the experimentation results.

4.3.3 Substitution.

The expanded series are substituted into the governing equations and simplified using the trigonometric identities and orthogonality to form two sets of nonlinear algebraic equations with two sets of unknowns (w_{ij} and f_{ij}).

$$\begin{aligned}
I_{ij}^e w_{ij} = & -t \bar{\sigma}_{yy} \left(\frac{j\pi}{b} \right)^2 \xi_{ij} - q_{ij}^c - \sum_k \sum_l t \kappa_x \left(\frac{l\pi}{b} \right)^2 \frac{16ij}{\pi^2 (i^2 - k^2)(j^2 - l^2)} f_{kl} \\
& + \sum_k \sum_l \sum_m \sum_n \\
& \left\{ \left| \frac{1}{4} \left[(-II_{klmn}^e - III_{klmn}^e - IV_{klmn}^e - V_{klmn}^e) \beta_{kl} w_{kl} + (VI_{klmn}^e - VII_{klmn}^e) f_{kl} (w_{mn} + \xi_{mn}) \right] \right| \right. \\
& + \left| \frac{1}{4} \left[(II_{klmn}^e + III_{klmn}^e - IV_{klmn}^e - V_{klmn}^e) \beta_{kl} w_{kl} + (-VI_{klmn}^e - VII_{klmn}^e) f_{kl} (w_{mn} + \xi_{mn}) \right] \right| \\
& - \left| \frac{1}{4} \left[(II_{klmn}^e + III_{klmn}^e - IV_{klmn}^e - V_{klmn}^e) \beta_{kl} w_{kl} + (-VI_{klmn}^e - VII_{klmn}^e) f_{kl} (w_{mn} + \xi_{mn}) \right] \right| \\
& + \left| \frac{1}{4} \left[(II_{klmn}^e - III_{klmn}^e + IV_{klmn}^e - V_{klmn}^e) \beta_{kl} w_{kl} + (-VI_{klmn}^e - VII_{klmn}^e) f_{kl} (w_{mn} + \xi_{mn}) \right] \right| \\
& - \left| \frac{1}{4} \left[(II_{klmn}^e - III_{klmn}^e + IV_{klmn}^e - V_{klmn}^e) \beta_{kl} w_{kl} + (-VI_{klmn}^e - VII_{klmn}^e) f_{kl} (w_{mn} + \xi_{mn}) \right] \right| \\
& + \left| \frac{1}{4} \left[(-II_{klmn}^e + III_{klmn}^e + IV_{klmn}^e - V_{klmn}^e) \beta_{kl} w_{kl} + (VI_{klmn}^e - VII_{klmn}^e) f_{kl} (w_{mn} + \xi_{mn}) \right] \right| \\
& + \left| \frac{1}{4} \left[(-II_{klmn}^e + III_{klmn}^e + IV_{klmn}^e - V_{klmn}^e) \beta_{kl} w_{kl} + (VI_{klmn}^e - VII_{klmn}^e) f_{kl} (w_{mn} + \xi_{mn}) \right] \right| \\
& - \left| \frac{1}{4} \left[(-II_{klmn}^e - III_{klmn}^e - IV_{klmn}^e - V_{klmn}^e) \beta_{kl} w_{kl} + (VI_{klmn}^e - VII_{klmn}^e) f_{kl} (w_{mn} + \xi_{mn}) \right] \right| \\
& - \left| \frac{1}{4} \left[(-II_{klmn}^e - III_{klmn}^e - IV_{klmn}^e - V_{klmn}^e) \beta_{kl} w_{kl} + (VI_{klmn}^e - VII_{klmn}^e) f_{kl} (w_{mn} + \xi_{mn}) \right] \right| \left. \right\}
\end{aligned}$$

where:

$$\begin{aligned}
I_{ij}^e &= D_{11} \left(\frac{i\pi}{a} \right)^4 + 2(D_{12} + 2D_{66}) \left(\frac{i\pi}{a} \right)^2 \left(\frac{j\pi}{b} \right)^2 + D_{22} \left(\frac{j\pi}{b} \right)^4 + k_{xx} \\
&\quad + k_{xz} \left(\frac{i\pi}{a} \right)^2 + k_{yz} \left(\frac{j\pi}{b} \right)^2 + t\bar{\sigma}_{yy} \left(\frac{j\pi}{b} \right)^2 \\
II_{klmn}^e &= D_{11} \left(\frac{m\pi}{a} \right)^4 + 2(D_{12} + 2D_{66}) \left(\frac{m\pi}{a} \right)^2 \left(\frac{n\pi}{b} \right)^2 + D_{22} \left(\frac{n\pi}{b} \right)^4 \\
&\quad + D_{11} \left(\frac{k\pi}{a} \right)^2 \left(\frac{m\pi}{a} \right)^2 + D_{12} \left(\frac{k\pi}{a} \right)^2 \left(\frac{n\pi}{b} \right)^2 \\
&\quad + D_{12} \left(\frac{l\pi}{b} \right)^2 \left(\frac{m\pi}{a} \right)^2 + D_{22} \left(\frac{l\pi}{b} \right)^2 \left(\frac{n\pi}{b} \right)^2 \\
III_{klmn}^e &= 2D_{11} \left(\frac{k\pi}{a} \right) \left(\frac{m\pi}{a} \right)^3 + 2(D_{12} + 2D_{66}) \left(\frac{k\pi}{a} \right) \left(\frac{m\pi}{a} \right) \left(\frac{n\pi}{b} \right)^2 \\
IV_{klmn}^e &= 2D_{22} \left(\frac{l\pi}{b} \right) \left(\frac{n\pi}{b} \right)^3 + 2(D_{12} + 2D_{66}) \left(\frac{l\pi}{b} \right) \left(\frac{m\pi}{a} \right)^2 \left(\frac{n\pi}{b} \right) \\
V_{klmn}^e &= 4D_{66} \left(\frac{k\pi}{a} \right) \left(\frac{l\pi}{b} \right) \left(\frac{m\pi}{a} \right) \left(\frac{n\pi}{b} \right) \\
VI_{klmn}^e &= t \left[\left(\frac{k\pi}{a} \right)^2 \left(\frac{n\pi}{b} \right)^2 + \left(\frac{l\pi}{b} \right)^2 \left(\frac{m\pi}{a} \right)^2 \right] \\
VII_{klmn}^e &= 2t \left(\frac{k\pi}{a} \right) \left(\frac{l\pi}{b} \right) \left(\frac{m\pi}{a} \right) \left(\frac{n\pi}{b} \right)
\end{aligned} \tag{63}$$

$$\begin{aligned}
I_{ij}^c f_{ij} = & \bar{\sigma}_{yy} \left(A_{12}^* \left(\frac{j\pi}{b} \right)^2 + A_{22}^* \left(\frac{i\pi}{a} \right)^2 \right) \alpha_{ij}^* \\
& + \sum_p \sum_q \kappa_x \left(\frac{q\pi}{b} \right)^2 \frac{16pq}{\pi^2 (p^2 - i^2)(q^2 - j^2)} W_{pq} \\
& + \sum_k \sum_l \sum_m \sum_n \\
& \left\{ \left\| \frac{1}{4} \left[(-II_{klmn}^c + III_{klmn}^c + IV_{klmn}^c - V_{klmn}^c) \alpha_{kl} f_{mn} \right] \right\|_{i=k-m \atop j=l-n} \right. \\
& + \left\| \frac{1}{4} \left[(-II_{klmn}^c - III_{klmn}^c + IV_{klmn}^c + V_{klmn}^c) \alpha_{kl} f_{mn} \right] \right\|_{i=k-m \atop j=l+n} \\
& + \left\| \frac{1}{4} \left[(-II_{klmn}^c + III_{klmn}^c - IV_{klmn}^c + V_{klmn}^c) \alpha_{kl} f_{mn} \right] \right\|_{i=k+m \atop j=l-n} \\
& \left. + \left\| \frac{1}{4} \left[(-II_{klmn}^c - III_{klmn}^c - IV_{klmn}^c - V_{klmn}^c) \alpha_{kl} f_{mn} \right] \right\|_{i=k+m \atop j=l+n} \right\} \\
& + \sum_p \sum_q \sum_r \sum_s \\
& \left\{ \left\| \frac{1}{4} \left[(VI_{pqrs}^c (w_{pq} + 2\xi_{pq}) - VII_{pqrs}^c w_{pq} - VIII_{pqrs}^c z_{pq}) w_{rs} \right] \right\|_{i=p+r \atop j=q+s} \right. \\
& + \left\| \frac{1}{4} \left[(VI_{pqrs}^c (w_{pq} + 2\xi_{pq}) - VII_{pqrs}^c w_{pq} - VIII_{pqrs}^c z_{pq}) w_{rs} \right] \right\|_{i=p-r \atop j=q-s} \\
& + \left\| \frac{1}{4} \left[(VI_{pqrs}^c (w_{pq} + 2\xi_{pq}) + VII_{pqrs}^c w_{pq} + VIII_{pqrs}^c z_{pq}) w_{rs} \right] \right\|_{i=p+r \atop j=q-s} \\
& \left. + \left\| \frac{1}{4} \left[(VI_{pqrs}^c (w_{pq} + 2\xi_{pq}) + VII_{pqrs}^c w_{pq} + VIII_{pqrs}^c z_{pq}) w_{rs} \right] \right\|_{i=p-r \atop j=q+s} \right\} \\
& \quad i, j = 0, 2, 4, \dots \\
& \quad k, l = 0, 2, 4, \dots \\
& \quad m, n = 0, 2, 4, \dots \\
& \quad p, q = 1, 3, 5, \dots \\
& \quad r, s = 1, 3, 5, \dots
\end{aligned} \tag{64}$$

where:

$$\begin{aligned}
I_{ij}^c &= A_{11}^* \left(\frac{j\pi}{b} \right)^4 + \left(2A_{12}^* + A_{66}^* \left(\frac{i\pi}{a} \right)^2 \right) \left(\frac{j\pi}{b} \right)^2 + A_{22}^* \left(\frac{i\pi}{a} \right)^4 \\
II_{klmn}^c &= A_{11}^* \left(\frac{l\pi}{b} \right)^4 + \left(2A_{12}^* + A_{66}^* \left(\frac{k\pi}{a} \right)^2 \right) \left(\frac{l\pi}{b} \right)^2 + A_{22}^* \left(\frac{k\pi}{a} \right)^4 + A_{12}^* \left(\frac{k\pi}{a} \right)^2 \left(\frac{n\pi}{b} \right)^2 \\
&\quad + A_{22}^* \left(\frac{k\pi}{a} \right)^2 \left(\frac{m\pi}{a} \right)^2 + A_{11}^* \left(\frac{l\pi}{b} \right)^2 \left(\frac{n\pi}{b} \right)^2 + A_{12}^* \left(\frac{l\pi}{b} \right)^2 \left(\frac{m\pi}{a} \right)^2 \\
III_{klmn}^c &= 2A_{11}^* \left(\frac{l\pi}{b} \right) \left(\frac{n\pi}{b} \right)^3 + \left(2A_{12}^* + A_{66}^* \right) \left(\frac{l\pi}{b} \right) \left(\frac{m\pi}{a} \right)^2 \left(\frac{n\pi}{b} \right) \\
IV_{klmn}^c &= \left(2A_{12}^* + A_{66}^* \right) \left(\frac{k\pi}{a} \right) \left(\frac{m\pi}{a} \right) \left(\frac{n\pi}{b} \right)^2 + 2A_{22}^* \left(\frac{k\pi}{a} \right) \left(\frac{m\pi}{a} \right)^3 \\
V_{klmn}^c &= A_{66}^* \left(\frac{k\pi}{a} \right) \left(\frac{l\pi}{b} \right) \left(\frac{m\pi}{a} \right) \left(\frac{n\pi}{b} \right) \\
VI_{pqrs}^c &= \frac{1}{t} \left(\frac{p\pi}{a} \right) \left(\frac{q\pi}{b} \right) \left(\frac{r\pi}{a} \right) \left(\frac{s\pi}{b} \right) \\
VII_{pqrs}^c &= \frac{1}{t} \left(\frac{p\pi}{a} \right)^2 \left(\frac{s\pi}{b} \right)^2 \\
VIII_{pqrs}^c &= \frac{1}{t} \left[\left(\frac{p\pi}{a} \right)^2 \left(\frac{s\pi}{b} \right)^2 + \left(\frac{r\pi}{a} \right)^2 \left(\frac{q\pi}{b} \right)^2 \right]
\end{aligned} \tag{65}$$

In equations 62 and 64, the terms within the double bars (||) are included only if the conditions of the subscripted equations after the term are satisfied.

These equations represent the energy and compatibility equations of the structural system.

4.3.4 Solution.

The governing equations are nonlinear and require an iterative procedure to reach a solution. The solutions for each governing equation are used for the next iteration. An under-relaxation factor (γ) may be used to help stabilize the solution process.

$$w_{ij}^{n+1} = w_{ij}^n + \gamma(g_1(w_{ij}^n, f_{ij}^n) - w_{ij}^n) \quad (66)$$

$$f_{ij}^{n+1} = f_{ij}^n + \gamma(g_2(w_{ij}^{n+1}) - f_{ij}^n) \quad (67)$$

where:

g_1 : represents the energy equation

g_2 : represents the compatibility equation

Convergence on a solution is determined by comparing successive iterative solutions. The change in the value of the current solution is compared to the value of the previous solution. A decrease in the error value indicates convergence. This error value is compared to a user set tolerance. When the error falls below this tolerance, the solution is considered converged.

$$w_{error}^{n+1} = \frac{\sqrt{(w_{11}^{n+1} - w_{11}^n)^2 + (w_{13}^{n+1} - w_{13}^n)^2 + \dots + (w_{ij}^{n+1} - w_{ij}^n)^2}}{\sqrt{(w_{11}^n)^2 + (w_{13}^n)^2 + \dots + (w_{ij}^n)^2}} \quad (68)$$

The process for calculating the state of the plate under load involves both an iterative solution for each load and a subsequent increase in the load. The user sets the initial stress and the initial load step size. The code calculates a solution that meets the user-specified tolerances and increases the load accordingly. In the case where a converged solution cannot be found, the load step size is halved and another solution is attempted. This process is continued until the load step size is less than a minimum step size set by the user.

The load step solution is considered to be unsolved if (1) the error values increase (indicating divergence) consecutively more than a user set number of times or (2) the number of total iterations required is higher than a user set value.

The results from the code include the modal amplitudes for the initial shape of the facesheet (ξ), the stiffness factors of the facesheet (α, β) and for each load step, the out-of-plane deformation (w), the Airy stress in the plate (f), the complementary stress of the core (q^c), the far-field stress ($\bar{\sigma}_{yy}$), and errors of the converged solution (w_{error}, f_{error}) for each iteration.

This iterative method for finding a solution to the governing equations was implemented in the Fortran77 program GROWTH4 (the fourth version of the original GROWTH program written by Tsang [3]). The code listing for GROWTH4 can be found in reference 5.

The main differences between the original GROWTH and GROWTH4 are the ability to incorporate facesheet damage, through the use of regional facesheet stiffness factors, the advancing load step procedure, the convergence criteria, the discrete value sampling method, and the criteria for determining the complementary-core stress.

For parameters similar to those used in this program, the program code requires up to 1 minute per iteration and several hours for an entire solution using a PC with a 300 MHz Pentium II processor.

4.3.5 Results.

Several analytical models were solved to compare the model results to the actual test data and to look at the effects of different parameters on the damage growth behavior. These studies include the effect of panel width, curvature, and facesheet damage size. The detailed analytical results are included in reference 5.

Figure 44 compares the experimental gage no. 2 stress-strain data of a 152-mm flat panel (F6-3). The analysis method does capture the general behavior of the panel, with an increased strain indicating lateral propagation of the indentation. In comparison to the experimental data, the analysis predicts a slightly higher damage growth stress and a significantly lower ultimate stress.

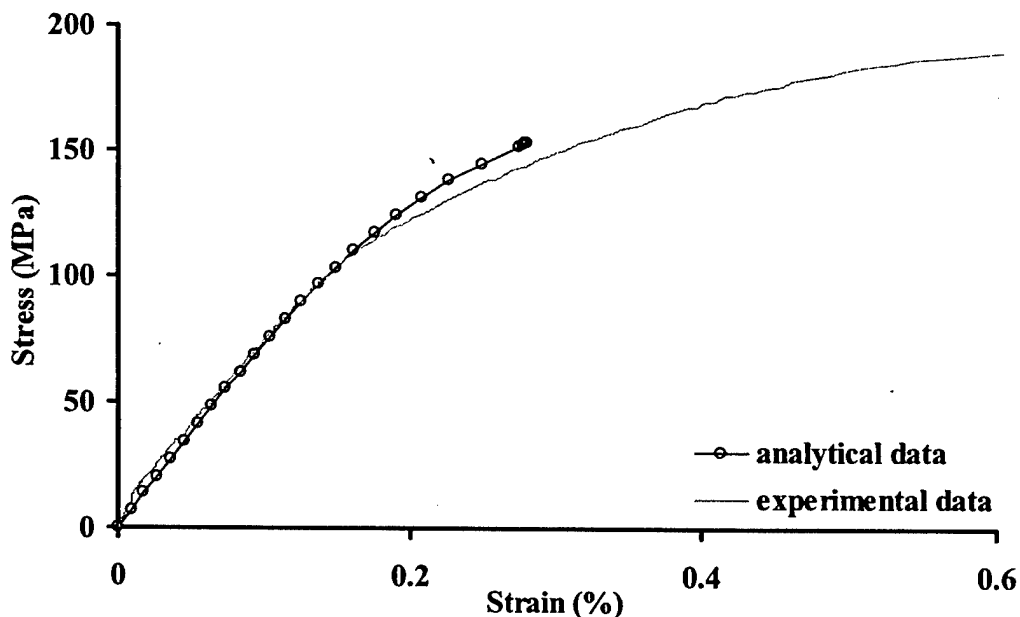


FIGURE 44. ANALYTICAL VS EXPERIMENTAL RESULTS

Figure 45 shows the effect of width on the damage growth behavior of the analytical model. It is apparent that the models with smaller widths (82.6 and 102 mm) show a slightly lower ultimate stress and damage growth stress. There also appears to be less difference between the wider models (152 and 203 mm).

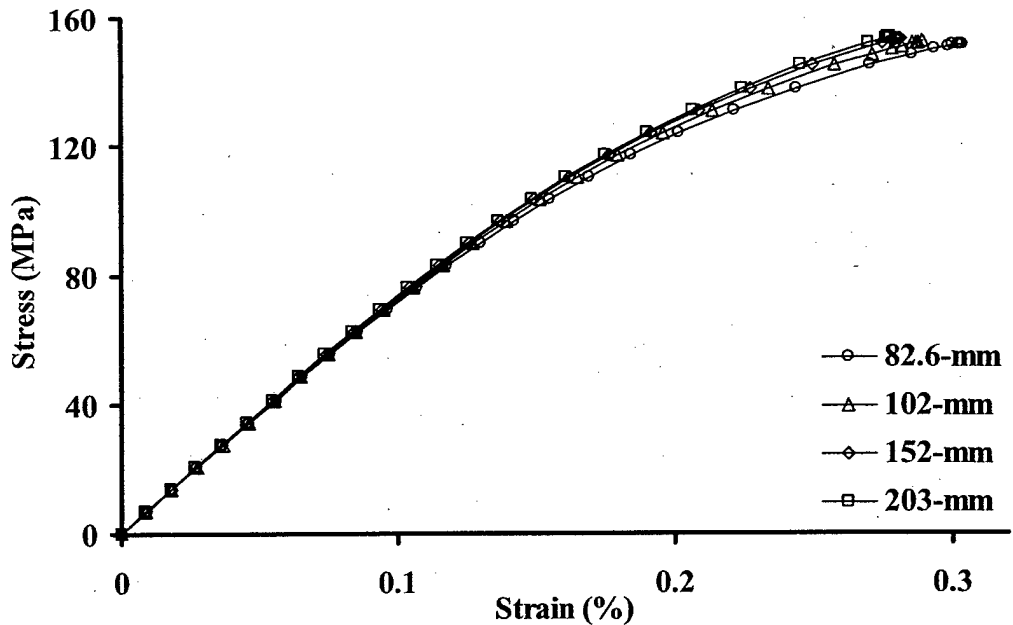


FIGURE 45. MODEL WIDTH EFFECTS ON DAMAGE GROWTH

The effect of panel curvature on the model damage growth is shown in figure 46. There does not appear to be any significant difference in either the ultimate stress or the growth stress between panels of different curvatures (all other parameters being equal).

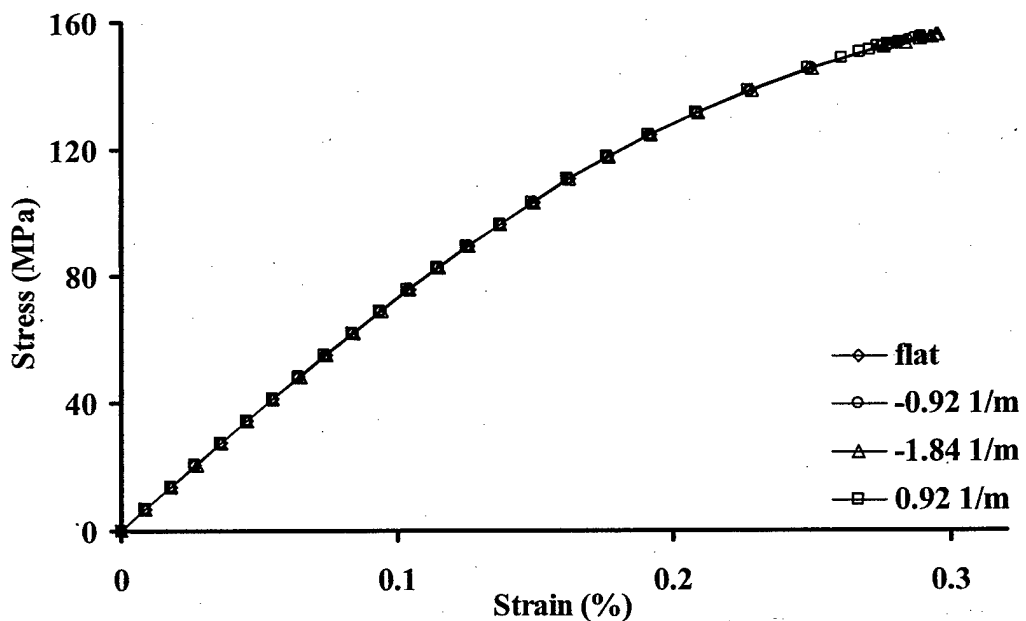


FIGURE 46. MODEL CURVATURE EFFECTS ON DAMAGE GROWTH

To look at the effect of facesheet damage size on the damage growth behavior of the model, several different solutions were obtained for panels with different damage sizes. In these runs, only the membrane stiffness of the facesheet is affected. A degradation of 30% is inflicted at the center of the damage region. This damage extent is held constant while the size of the damage region is increased. The proportional shape of the damage region is maintained with the width (x direction) of the damage region being 1.5 times the length (y direction), similar to that seen in the experiments. The results (figure 47) indicate that the ultimate stress and damage growth stress actually increase very slightly with an increased "membrane" damage size. In other words, the decrease in material moduli at the damage site cause the load to shift to the unloaded portion of the panel.

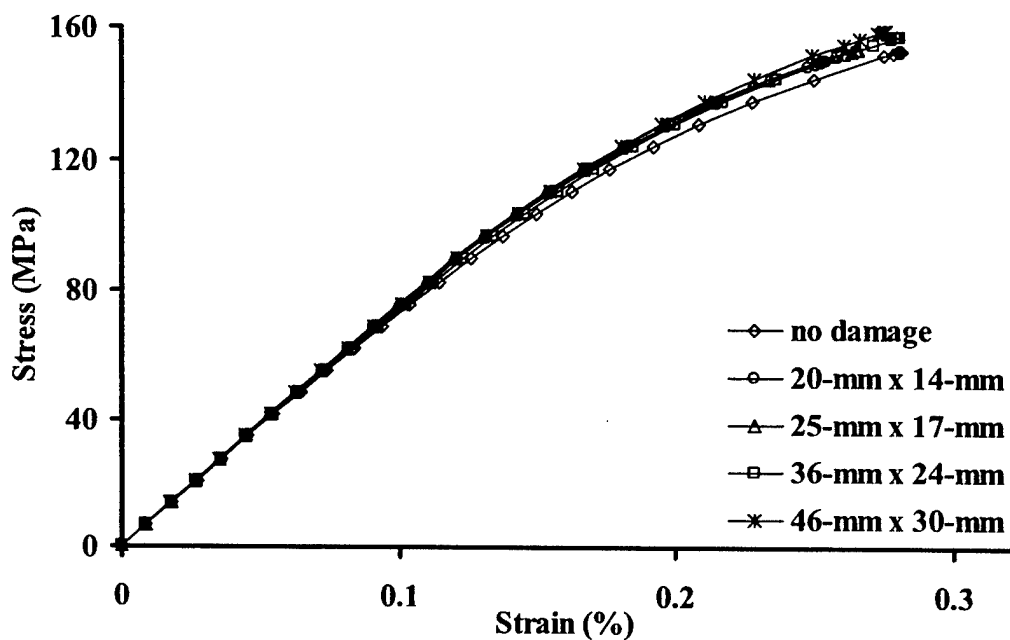


FIGURE 47. MODEL MEMBRANE DAMAGE SIZE EFFECTS ON DAMAGE GROWTH

The model had some problem converging on membrane damage levels exceeding 30%. Solutions for models with more extensive damage may be possible by manipulating some of the other input parameters such as the under-relaxation factor or modes in the x and y direction.

The results from the "bending" damage study are shown in figure 48. These solutions are for panels with a bending stiffness degradation of 50%. The size of the facesheet damage region is increased as before with the shape of the damage region remaining constant. The results show that for panels with larger bending damage regions, the ultimate stress and damage growth stress decrease.

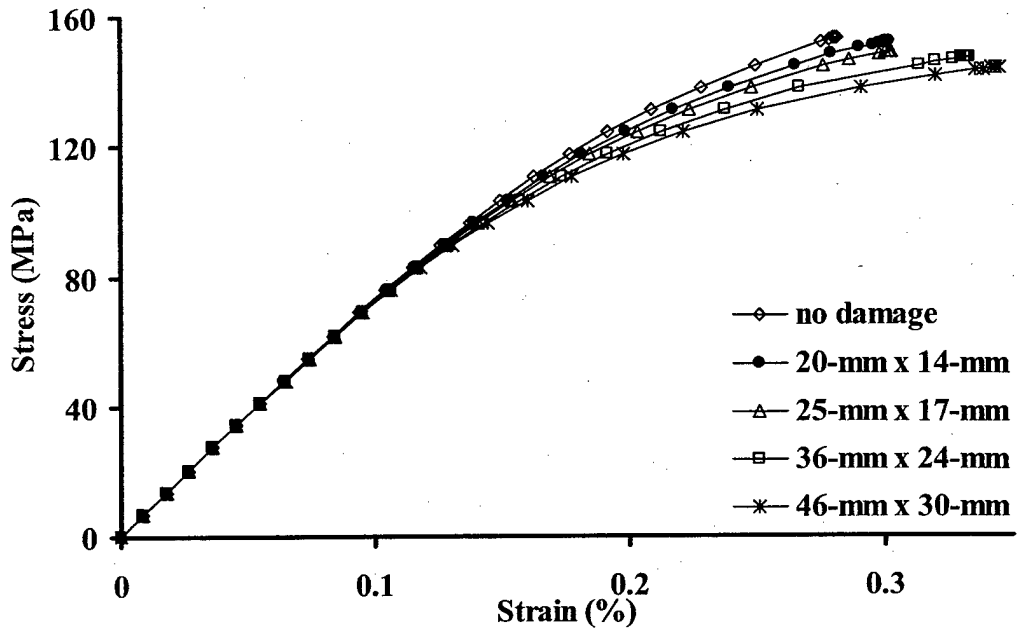


FIGURE 48. MODEL BENDING DAMAGE SIZE EFFECTS ON DAMAGE GROWTH

The damage arrest mechanism that was observed and measured in the CAI tests is also apparent in the analysis results (figure 49). All of the analysis results indicated a damage arrest width of approximately 50 mm.

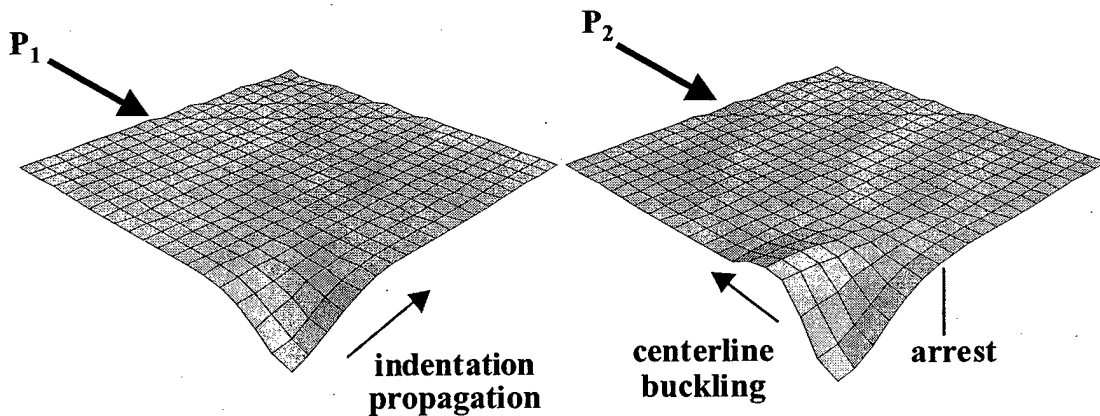


FIGURE 49. DAMAGE ARREST MECHANISM ($P_1 < P_2$)

Models with different damage levels indicated a consistent width for the maximum extent of the damage propagation (figures 50 to 52).

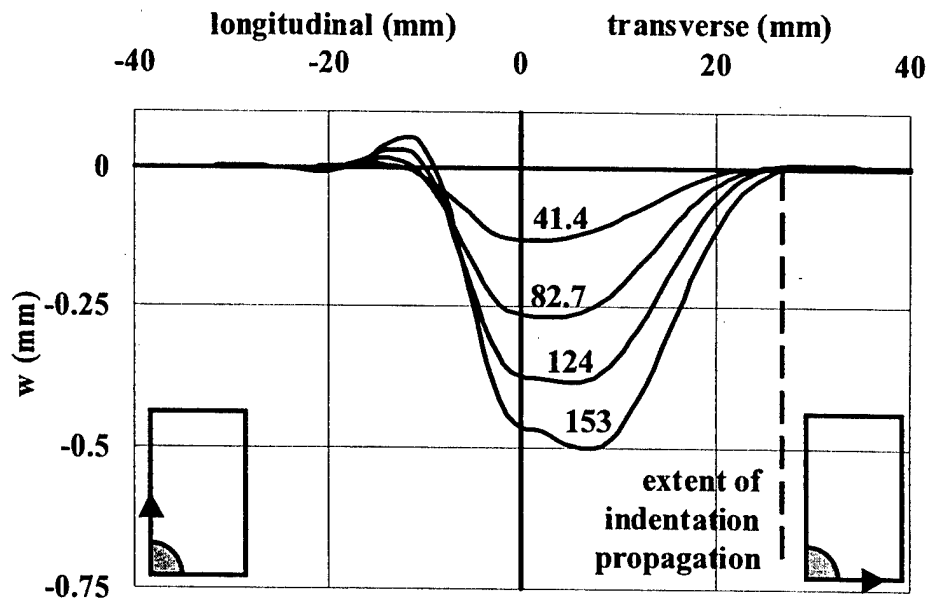


FIGURE 50. OUT-OF-PLANE DEFORMATION OF THE FLAT 152-mm MODEL WITHOUT FACESHEET DAMAGE

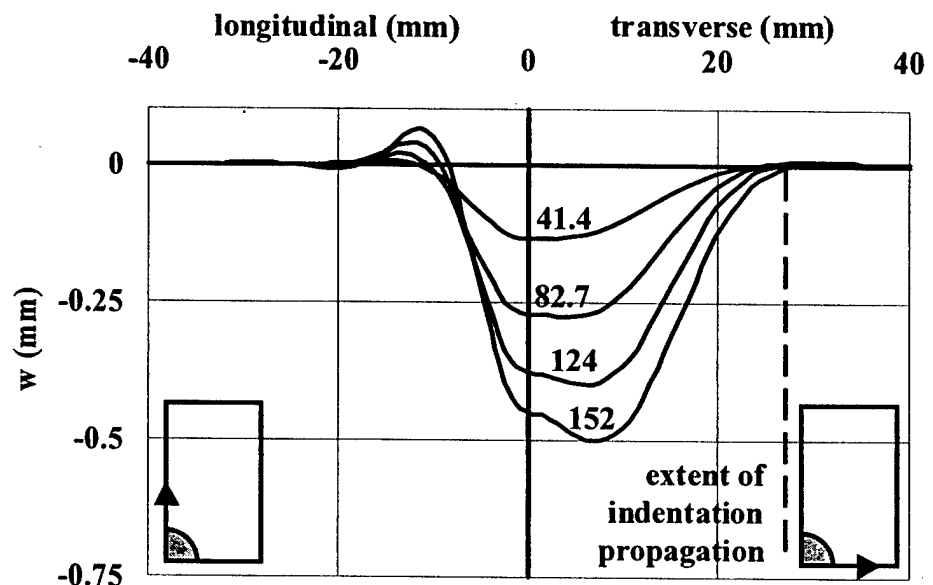


FIGURE 51. OUT-OF-PLANE DEFORMATION OF THE FLAT 152-mm MODEL WITH FACESHEET DAMAGE

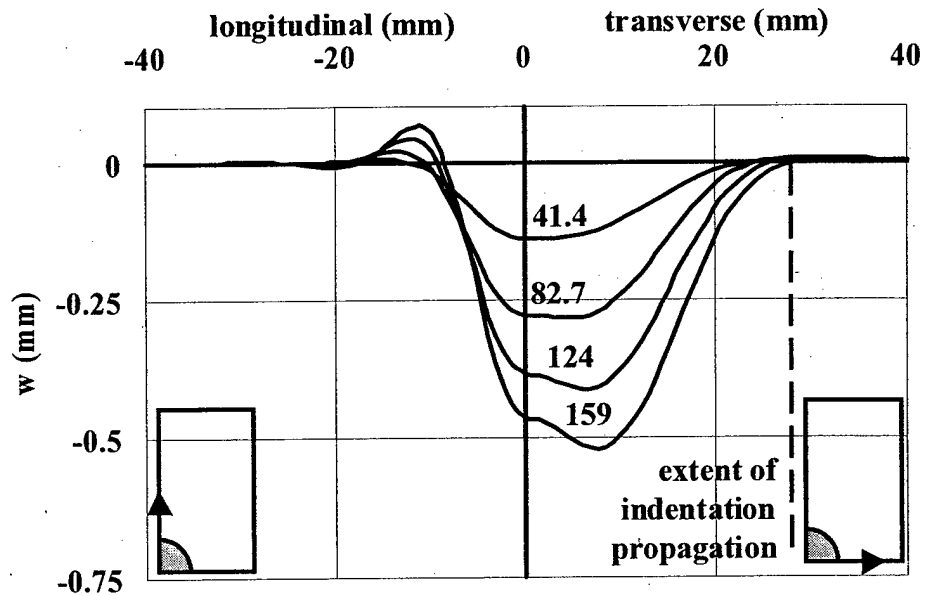


FIGURE 52. OUT-OF-PLANE DEFORMATION OF THE FLAT 83-mm MODEL WITHOUT FACESHEET DAMAGE

4.3.6 Required Input Parameters.

The collection of input parameters required by this analytical tool serves to summarize its development. The damage resulting from an impact is characterized by four separate damage types: facesheet indentation, facesheet stiffness degradation, facesheet/core disbond, and crushed core. For each of these types of damage, the associated elliptical region must be determined as well as changes in the appropriate constitutive relationships.

Facesheet indentation can be determined explicitly by measuring the depth of the facesheet, relative to some reference point. The depths can be used directly if known at the nodal points or indirectly to fit a surface to the values as is done in this report. Although discrete points are needed, the approach herein is to assume an elliptical region with a \cos^8 shape function and a maximum center deflection.

Facesheet indentation can be determined explicitly by determining the depth of the facesheet, relative to some reference point either through sectioning and surface measurement. The depths can be used directly, if known, at the nodal points or indirectly to fit a surface to the values as is done in this report. Although discrete points are needed, the approach herein is to assume an elliptical region with a \cos^8 shape as the interpolation function. Thus, all that would be required is the minor and major axis of the ellipse and the center depth. The use of \cos^8 interpolation function reduces the number of input values as well, provided that it is an accurate representation of the indentation.

Facesheet/core disbond may be assumed for physical debonding in the damage area or to account for cores that, once crushed, offer little or no resistance to the facesheet up to the depth of the

original crushing. Again, the model requires discrete points, but in the present implementation, an elliptical region with a \cos^8 shape function is assumed with a maximum center deflection. Sectioning and inspecting impacted panels determined these values.

Facesheet stiffness degradation may result from detailed analysis of the damage state of the facesheet and the corresponding stiffness degradation. The model separates the in-plane stiffness from the bending stiffness using α and β , respectively. Again, the model requires discrete points; however, an elliptical region with a \cos^8 shape function is assumed with a maximum degradation at the center. No empirical methods were employed in the present implementation to derive these values.

In addition to the damage state, the constitutive relationships must be known for the undamaged facesheet, undamaged core, and damaged core. Note that the damage in the facesheet is accounted by a reduction in the in-plane and/or bending stiffness. The constitutive properties of the undamaged facesheet and core should be known; whereas, the stiffness of damaged core needs to be determined. This can be done via a flat-wise compression test that will result in the ultimate normal stress, plateau stress, and relaxation modulus as shown in figure 41.

4.3.7 Model Output.

The modified model provides the nonlinear response of the impacted facesheet under uniaxial compression. Growth of the indentation is modeled by further deflection of the facesheet into the core. In addition, the stress and strain states in the facesheet can be determined and used in appropriate failure criteria. The analysis may also provide some indication of indentation arrest as indicated in section 4.3.5.

5. DISCUSSION.

Several aspects of damage tolerance behavior (including impact damage characteristics, damage growth, and ultimate strength) were revealed through the observations, measurements, and analysis made during this research. The discussion of these aspects follows.

The initial intent of this research was to focus exclusively on damage tolerance issues. By removing the effects of damage resistance, it was assumed that factors affecting damage tolerance would become more apparent. The effects of damage resistance were expected to be negated by keeping constant the amount of damage inflicted to each panel. Prior to impact, the total potential energy of the impacting device was used as a controlling parameter (equation 1). First, the amount of energy required to cause BVID to a standard size specimen (83 mm) was determined. This energy was held constant for all impacted specimens. The different global-bending stiffness of the CAI specimens of different sizes resulted in unequal impact damage. The panels with higher global-bending stiffness suffered more extensive damage (figures 5 and 6).

Damage resistance is dependent upon not only the core properties and the facesheet material and layup, but also upon the global geometry of the panel and the boundary conditions during the impact event. Therefore, damage resistance became an important factor in this research.

The residual indentation and crushed core appeared to be the damage modes that contributed most to the specimen's CAI behavior. Impact damage growth was observed in the form of propagation of the initial indentation, perpendicular to the loading direction. All CAI specimens displayed this type of damage growth. Strain gages, placed lateral to the initial damage (figure 21), confirmed the observed growth, with the gage closest to the damage recording a nonlinear response to the compressive load. This nonlinear response indicated damage/indentation growth to the strain gage location.

GROWTH4 analysis results displayed similar CAI behavior as that observed during testing. The indentation grows perpendicular to the loading direction, as the facesheet at the edge of the indentation buckles inward. When the stress in the facesheet bypasses the damage, the local buckling is caused by the initial eccentricity of the facesheet as well as a stress concentration at the edge of the indentation.

The damage growth behavior of the standard width specimens (83 mm) differed from the wider specimens (152 and 305 mm). For the standard specimens, the damage grew laterally until the panel suffered a catastrophic wrinkling across the center of the damage, perpendicular to the loading direction.

For the wider specimens, the indentation appeared to grow slowly until the edges of the now elongated indentation reached approximately 38 mm from the center of the damage. At this point, the indentation no longer grew in the lateral direction. The bulges above and below the indentation grew larger before the ultimate failure of the specimen. This damage-arrest behavior was also captured by the local strain measurements. The strain gage data show that the damage grows until it is first detected by gage no. 2 (located 25.4 mm from the center of the damage). For all wide panels, gage no. 3 shows little or no nonlinear response, indicating that the damage does not spread beyond its location (38.1 mm from the center of the damage).

This damage-arrest behavior was also present in the GROWTH4 analysis results. First, lateral indentation was seen in the plate representing the facesheet. Then, at approximately 40 mm, the buckling mode of the facesheet changed from a local first-order buckling mode to a higher order buckling mode along the centerline of the facesheet (figure 49).

The ultimate strength appeared to be independent of the panel geometry for all the wide panels (152 and 305 mm). The standard width specimens (83 mm) failed at approximately 85% of the ultimate strength of the wide specimens. Because the wide panels suffered different levels of impact damage, dependent upon their global geometry, this indicated that for the wide panels, the ultimate strength is also independent of the initial damage state. The standard width specimens failed at a lower ultimate stress due to the proximity of the panel edge to the maximum extent of the damage growth.

The ultimate strength appears to be dependent only upon the extent of the maximum damage propagation (and arrest), which itself is independent upon the global geometry. The ultimate strength of the standard width specimens is affected by the proximity of the edge to the maximum damage propagation and, therefore, increases the stress concentration at the net section

and has a lower maximum stress. The wider panels (152 and 305 mm) are not affected by this edge effect.

The damage growth stress of a specimen was defined in this program as the far-field stress at which a strain gage located 25.4 mm from the center of the damage begins to show a nonlinear strain response due to the lateral growth of the impact damage. The onset of damage growth, as measured by gage no. 2 (damage growth stress), initially appeared to be a function of the global bending stiffness of the panel, with the stiffer panels having higher damage growth stress (figure 29). Analysis demonstrated that this was only an indirect correlation. In fact, the damage growth stress is a function of the initial damage state of the specimens. The impact damage to the facesheet is in the form of matrix cracking, delamination, and fiber breakage, all acting to create a more compliant region around the impact location. The panels with higher global-bending stiffness suffer more extensive damage in an impact event of similar energy. This compliant region acts to soften the area near the residual indentation where damage propagation initiates with local buckling. The more extensive facesheet damage of the stiffer panels results in greater softening and lower local stresses in this critical area. This results in a delayed initiation of the damage propagation.

Figure 53 shows results from the GROWTH4 analysis. Run01a represents a flat panel with no facesheet material damage, Run03d represents a flat panel with facesheet material damage, included as a local compliant region in the membrane stiffness of the facesheet. The contours shown display the stress concentrations in the facesheet. Because of the local softening of the facesheet, Run03d displays a slightly lower stress concentration at the edge of the indentation (1.17 vs 1.19). This lower stress concentration results in a delay of the damage growth seen in the panels with more extensive facesheet damage. A model with more extensive membrane damage may display a greater difference in the stress concentration among panels with different initial damage states.

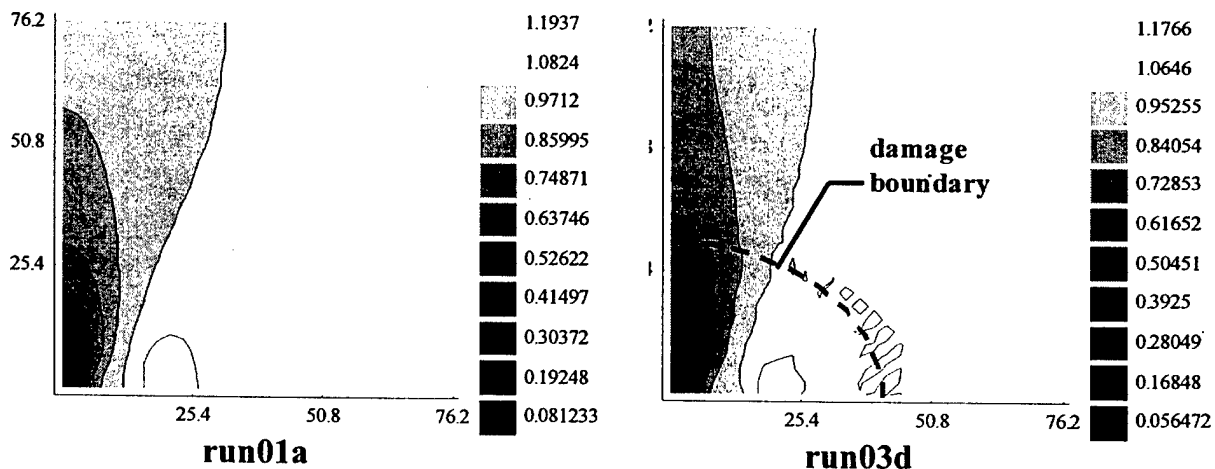


FIGURE 53. THE EFFECT OF LOCAL MEMBRANE COMPLIANCE ON THE STRESS CONCENTRATION

The behavior of each panel under load is summarized in figure 54. This figure shows the relationship of the growth, arrest, and ultimate loads between panels of different types. The gray region represents the facesheet damage, and the indentation is shown as the black region. The standard width specimen demonstrated indentation growth followed by the ultimate stress (with no damage arrest behavior observed). The lower ultimate stress of the standard width specimens was caused by the proximity of the panel edge to the damage region. The compliant specimen represents the panels with lower out-of-plane bending stiffness and lower facesheet damage. Such panels have a higher damage-growth stress than the standard width specimens, but do exhibit an indentation arrest behavior before the ultimate stress. The stiff specimen represents the panels with higher out-of-plane bending stiffness and higher facesheet damage. The panels also exhibit damage growth, but it occurs at a higher stress than either the compliant or standard specimen (caused by the larger facesheet damage region). Indentation arrest is also present with the maximum width of indentation propagation being approximately equal to the compliant specimens. The ultimate stress of the stiff specimens is approximately equal to that of the compliant specimens.

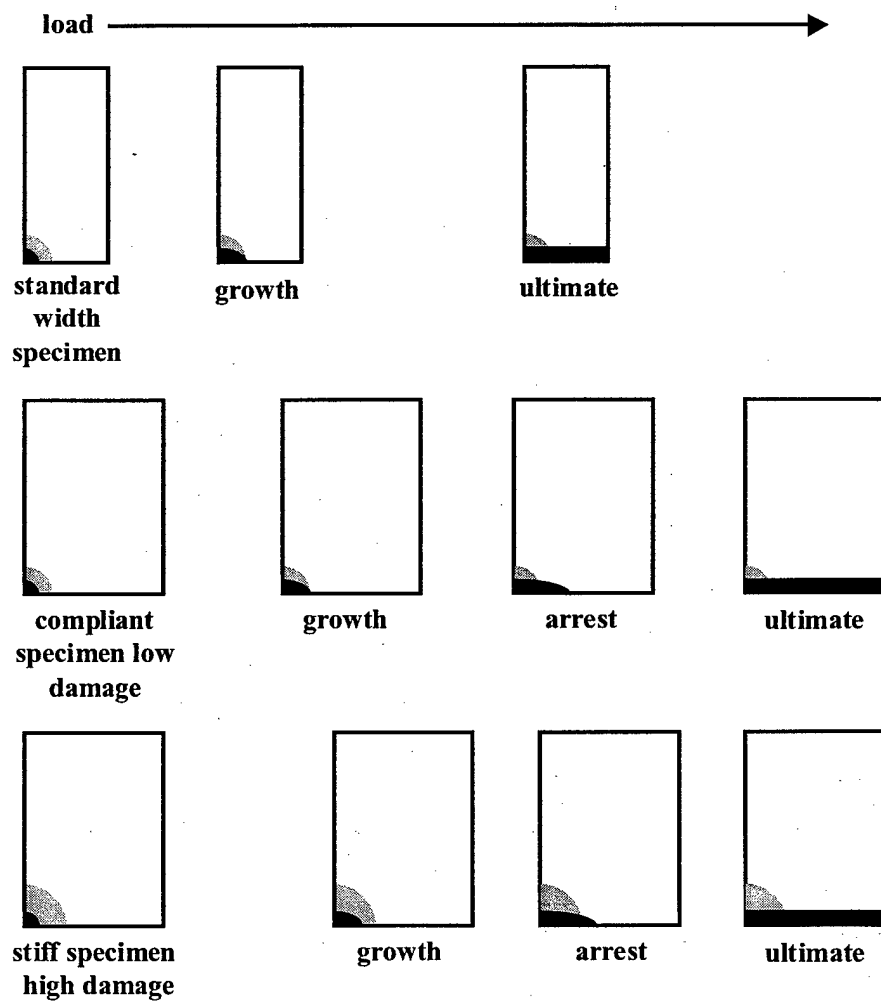


FIGURE 54. SUMMARY OF PANEL BEHAVIOR

The GROWTH4 method of analysis proved to be useful in determining the cause of the CAI behavior observed during the testing, including the damage growth, damage arrest, ultimate strength, and damage growth stress. The addition of the membrane and bending local stiffness reduction to represent material damage provides for a model that includes more of the factors affecting the damage tolerance of impacted specimens. Some difficulties with the model remain. For large panels with small damage regions, the analysis requires a large number of sampling points, resulting in long solution times. The inclusion of facesheet material damage affects the conversion behavior of iterations, also increasing the time required to reach a solution. The current method of iteration also prevents convergence for models with high factors of facesheet damage.

6. CONCLUSIONS AND RECOMMENDATIONS.

The experimental and analytical work contained here was successful in bringing to light some of the behavior of compression after impact (CAI) specimens of varying geometries. The following specific conclusions were reached.

1. The global geometry of the panel had a significant effect on the initial damage state of the impacted specimen.
2. Compression after impact behavior of thin gage sandwich panels with impact damage included an indentation propagation perpendicular to the loading direction. This behavior was confirmed by the strain gage measurements and the analysis.
3. Impacted specimens with widths of 152 mm or greater display a damage-arrest mechanism in which the indentation propagation arrests. This damage-arrest mechanism is independent of the initial damage state.
4. The ultimate strength of standard width specimens (83 mm) is less than that of wider specimens. This is caused by the stress redistribution around the damage region being affected by the free edges of the specimens. CAI testing indicated that 152-mm-wide specimens were not influenced by this finite width effect.
5. The ultimate strength of the wide specimens (152 and 305 mm) were not dependent upon either the global geometry or the initial damage state of the specimen. The ultimate strength is affected by the maximum extent of the damage growth, which is the same for all wide specimens.
6. Damage growth stress is dependent upon the initial damage state of the specimen. The more extensive damage suffered by the panels with greater global-bending stiffness created a larger compliant region around the indentation. This compliant softened the stress at the edge of the residual indentation, delaying the local buckling and damage growth.
7. The global geometry (width and curvature) of specimens larger than a standard size did not affect the damage tolerance of impacted composite sandwich specimens.

8. The developed analysis method and the associated software GROWTH4 provides for the inclusion of factors that closely represent the initial damage state of the specimen and influence the CAI behavior.

Based on problems and difficulties encountered in the study, the following recommendations are offered.

1. For studies focusing on damage tolerance, other test methods may be more successful at creating impact damage to the specimens and negating the effects of global geometry. Static indentation has been used with good repeatability and creates damage that is not dependent upon the global-bending stiffness of the panels. Another possible method is to support the back facesheet of the panel over its entire area, thus canceling the effects of global geometry.
2. The extent of the damage propagation, upon which the ultimate strength of a damage panel is dependent, appears to be an important characteristic of damage tolerance of sandwich panels. Because of the standard layups and impact energy used in this program, the factors that affect this damage propagation width were not clear. Further investigation of the factors that affect this trait would reveal additional information concerning damage tolerance (especially ultimate strength). The actual dimensions of the maximum damage growth might best be measured using the Moiré methods instead of relying on the discrete locations of the strain gages. The developed code may also be useful for this work as well.
3. The developed code predicts the failure of the specimen by an unstable growth of the damage indentation. It may be feasible to include more detailed failure criteria into the code, such as ply-by-ply box stress criteria. In addition, the current method of iteration is not capable of finding solutions to models with high factors of facesheet damage.

7. REFERENCES.

1. Moody, R.C. and Vizzini, A. J., "Damage Tolerance of Composite Sandwich Structures," DOT/FAA/AR-99/91, January 1999.
2. Kassapoglou, C. and Abbott, R., "A Correlation Parameter for Predicting the Compressive Strength of Composite Sandwich Panels After Low Speed Impact," AIAA/ASME/ASCE/AHS/ASC 20th Structures, Structural Dynamics, and Materials Conference, 1986, pp. 642-650.
3. Tsang, P.H. Wilson, "Impact Resistance and Damage Tolerance of Composite Sandwich Panels," Ph.D. Thesis, Massachusetts Institute of Technology, June 1994.
4. Minguet, P.J., "A Model for Predicting the Behavior of Impact Damaged Minimum Gage Sandwich Panels Under Compression," AIAA/ASME/ASCE/AHS/ASC 32nd Structures, Structural Dynamics and Materials Conference, Baltimore, Maryland, 1991, pp. 1112-1122.

5. Moody, R. Clifton, "Damage Tolerance of Impacted Composite Sandwich Panels," MS Thesis, Aerospace Engineering, University of Maryland, May 2001.
6. Vizzini, A.J., "An Efficient Algorithm to Characterize Stress-Strain Data Using Piecewise Linear Curves," *Journal of Testing and Evaluation*, Vol. 20, No. 2, March, 1992, pp. 126-131.
7. Selvadurai, A.P.S., *Elastic Analysis of Soil-Foundation Interaction*, Elsevier Scientific Publishing Company, 1979.
8. Press, W.H., Flannery, B.P., Teukolsky, S.A., and Vetterling, W.T., *Numerical Recipes*, Cambridge University Press, 1989.